frontiers | Frontiers in Earth Science

TYPE Original Research
PUBLISHED 12 January 2023
DOI 10.3389/feart.2022.1067012

OPEN ACCESS

EDITED BY
Dmitri Rouwet,
Istituto Nazionale di Geofisica e Vulcanologia, sezione di Bologna, Italy

REVIEWED BY
Gilles Levresse,
National Autonomous University of Mexico, Mexico
Teresa Scolamacchia,
A.S.S.E.T. -Regione Puglia, Italy

*CORRESPONDENCE
Cristian Montanaro,
✉ cristian.montanaro@min.uni-muenchen.de

SPECIALTY SECTION
This article was submitted to Volcanology, a section of the journal Frontiers in Earth Science

RECEIVED 11 October 2022
ACCEPTED 28 December 2022
PUBLISHED 12 January 2023

CITATION
Montanaro C, Ray L, Cronin SJ, Calibugan A, Rott S, Bardsley C and Scheu B (2023), Linking top and subsoil types, alteration and degassing processes at Rotokawa geothermal field, New Zealand.
Front. Earth Sci. 10:1067012.
doi: 10.3389/feart.2022.1067012

Linking top and subsoil types, alteration and degassing processes at Rotokawa geothermal field, New Zealand

Cristian Montanaro[1,2]*, Lena Ray[2], Shane J. Cronin[2], Aimee Calibugan[3], Stefanie Rott[1], Candice Bardsley[3] and Bettina Scheu[1]

[1]Department of Earth and Environmental Sciences, Ludwig-Maximilians-Universität München, Munich, Germany, [2]School of Environment, University of Auckland, Science Centre, Auckland, New Zealand, [3]Mercury NZ Ltd., Auckland, New Zealand

Surface geothermal expressions such as mud pools, fumaroles, mineral deposits, collapse pits, and hydrothermal eruption craters vary in scale and type over space and time. The evolution in space and time of these surficial thermal features strongly relates to alteration processes caused by hydrothermal fluids. The changes in the physical and mechanical properties of top and subsoils that can control fluid flow, degassing patterns, and occurrence of geothermal hazards remain understudied. The thermal area located south of the Rotokawa geothermal field (New Zealand) includes a variety of major natural surface thermal features and widespread sulphur deposits precipitated by acid–sulphate fluids in steam-heated zones. Decades of sulphur mining induced the formation of new thermal features. Such a setting represents an exemplary case study for investigating old and recently formed thermal features, soil characteristics, types and patterns of superposed hydrothermal alteration, and degassing processes. We combined field and laboratory methods to define groups of thermal features, soil types, and associated alteration. Their spatial distribution indicates that fluid circulation, alteration intensity, and degassing are strongly influenced by the local and regional geological and structural settings, as well as by mining activity. We found that at the water table level and within excavated areas, acidic fluids led to the deposition of mud deposits, sinters, and stromatolites around warm springs and mud pools. In the vadose, steam-heated portions, fluids generally leach and degrade the Taupo Pumice, resulting in broad unstable grounds and collapse structures, while extensive sulphur-encrusted grounds and sulphur-rich soils formed in excavated sites. In this framework, the degassing and fluid circulation within the top and subsoils are strongly affected by the dominant soil layer type, and in turn by its granulometry, texture, and alteration state. Our study of top and subsoils yields precious insights into surface expression variability, fluid–rock interaction processes, and sulphur deposition patterns within steam-heated zones. Processes at such a scale may strongly influence the migration of thermal manifestations, gas outputs, and ground subsidence within geothermal environments. From a broader perspective, our results will help assess the evolution of geothermal activity and related hazards in similar areas worldwide.

KEYWORDS

geothermal, top and subsoil, alteration, sulphur deposition, permeability, degassing activity

1 Introduction

Geothermal environments display a variety of thermal manifestations and alteration features produced by hydrothermal fluids. Variability in temperature, pressure, composition, and duration of alteration may affect the petrophysical and mechanical properties of rock and soil hosting hydrothermal fluids in such areas (Robb, 2004; Mormone et al., 2011; Pola et al., 2012; Frolova et al., 2014; Wyering et al., 2014; Heap et al., 2015; Mayer et al., 2015; Mormone et al., 2015; Frolova et al., 2016; Heap et al., 2017; Mayer et al., 2017; Mordensky et al., 2019; Frolova et al., 2020a; Revil et al., 2020; Kanakiya et al., 2021). Alteration and weakening/dissolution of rock and soil can promote permeability change, slope instability and mass wasting (Reid et al., 2002; John et al., 2008; Kristianto et al., 2013; Procter et al., 2014; Gvozdeva et al., 2015; Peruzzetto et al., 2019; Heap et al., 2021), and migration of thermal manifestations (Harris and Maciejewski, 2000; Ricci et al., 2015; Madonia et al., 2016; Montanaro et al., 2017; Frolova et al., 2019). Alteration also causes changes in surficial temperature and the hydrodynamic regime of a hydrothermal system (Dempsey et al., 2012; Rowland and Simmons, 2012; Kiryukhin et al., 2017) and may cause surface deformation and subsidence (Allis et al., 2009; Samsonov et al., 2011; Lynne et al., 2013; Koros et al., 2015; Basmanov et al., 2016). All of these processes may pose hazards to people within geothermal areas (e.g., those used for energy or tourism) and impact operational geothermal fields.

In dynamic geothermal settings, the formation and evolution of thermal features strongly relate to alteration processes affecting the properties of soil lithologies (Mayer et al., 2017; Frolova et al., 2020b). Thus, changes in physical and mechanical properties of the top and subsoils (i.e., the first decimetre to meters from the surface) play a key role in controlling degassing patterns by buffering and/or hindering the surficial thermal and gas outputs from the underlying hydrothermal system (Madonia et al., 2016; Heap et al., 2017; Montanaro et al., 2017; Frolova et al., 2019; Frolova et al., 2020a). However, so far, soil surveys in volcanic and geothermal areas have been exclusively used to estimate the budget of volatiles and identify and characterise active degassing structures sourcing the release of surficial gases, i.e., magmatic bodies and/or hydrothermal systems (Ármannsson et al., 2007; Chiodini et al., 2010; Carapezza et al., 2011; Shen et al., 2011; Pedone et al., 2015; Inguaggiato et al., 2018; Peiffer et al., 2018; Daskalopoulou et al., 2019; Taussi et al., 2019; Jentsch et al., 2020; Taussi et al., 2021). A few studies have considered the effect of i) subsoil heterogeneity on surficial degassing behaviour (Tassi et al., 2013; Bagnato et al., 2014; Bloomberg et al., 2014; Gresse et al., 2016; Montanaro et al., 2017) and ii) soil permeability in relation to the spatial and temporal distribution of thermal emission (Aubert et al., 2009; Schöpa et al., 2011; Harris et al., 2012; Heap et al., 2017; Mayer et al., 2017).

To better understand the link between soil types and alteration and degassing processes, we investigated the structure, composition, and alteration of the top and subsoils within the main thermal area of the Rotokawa geothermal field, New Zealand, managed by the Department of Conservation (DOC-thermal area; Figure 1). The many geothermal surface features include hot springs, fumaroles, extensive sulphur deposits, several areas of steaming ground, and hydrothermal eruption craters including the Lake Rotokawa itself (Collar and Browne, 1985; Krupp and Seward, 1987; Jones et al., 2000; Browne and Lawless, 2001; Rodgers et al., 2002; Milicich and Hunt, 2007). The surficial alteration (<200 m) at Rotokawa is driven by steam-heated acid-sulphate and bicarbonate fluids and is characterised near Lake Rotokawa by an intensive acidic assemblage (Krupp and Seward, 1987). Across the thermal field, the soil-forming deposits are mainly <2-kyr-old pyroclastic flows and fall units from the Taupo Volcano (Collar, 1985). Many of the old thermal features were reworked during sulphur mining activities, while new thermal features developed over the mined areas afterwards (Bardsley and Williams, 2017).

Here, we report results from field campaigns and laboratory analyses aimed at investigating i) the types and patterns of thermal expressions, ii) the top and subsoil lithologies and their alteration state, and iii) the control of soil types on fluid circulation and degassing.

2 Geological setting

The Rotokawa geothermal field is located in the central part of the Taupo Volcanic Zone in New Zealand (Figure 1), approximately 15 km northeast of the town of Taupo (Rowland and Simmons, 2012). Investigations in the 1960s identified a large high-temperature resource (>300 °C) with ~28 km^2 within the 30-Ωm resistivity contour (Figure 1; Risk 2000; McNamara et al., 2015). Structures aligned ~NE–SW, such as the Central and Injection Field Fault, supply deeper fluids into the hydrothermal system (Figure 1; Rowland et al., 2012; Wallis et al., 2013; Hopp et al., 2020; Calibugan et al., 2022). Rotokawa is a gas-rich high-temperature system (Giggenbach, 1995) with three aquifers: i) shallow meteoric groundwater in the first 100–300 m depth; ii) a complex intermediate aquifer between 300 and 1,000 m, with several different fluid types, including steam-heated groundwater, acid–sulphate–chloride fluids, and boiled reservoir (chloride) fluids; and iii) a chloride geothermal reservoir of >300°C below 1,000 m depth (Winick et al., 2009; Addison et al., 2015). Rotokawa emits 441 Mg d^{-1} of CO_2 and up to 31 Mg d^{-1} of H_2S (Bloomberg et al., 2014). The CO_2 and H_2S gases, coupled with boiling at shallow levels and mixing with shallow aquifer groundwater, yield acid–sulphate fluids above the upflow zones and bicarbonate fluids at the margins of the outflow. Shallow hydrothermal alteration is primarily due to acidic condensates, depositing large amounts of native sulphur in association with kaolinite, smectite, opal, and minor alunite (Krupp and Seward, 1987; Chambefort, 2021; Brooks-Clarke, 2021; Simpson et al., 2021). The main alteration assemblage in the deep reservoir is propylitic, formed by high-temperature, near-neutral pH chloride fluids. The alteration mineralogy includes quartz, chlorite, albite, illite, calcite, pyrite, and epidote, plus minor adularia, rare wairakite, and hematite (Krupp and Seward, 1987; Price et al., 2011; Simpson et al., 2021).

2.1 Geothermal features and subsurface geology

Thermal manifestations in the Rotokawa geothermal field (Figures 1, 2; Collar and Browne, 1985; Krupp and Seward, 1987; Bloomberg et al., 2014) are concentrated in two areas:

1) In the southern area, the most prominent thermal feature is the acid–sulphate (pH ~2) Lake Rotokawa (Te Reo Māori for "bitter lake") that occupies a hydrothermal eruption crater partly filled by the <2-kyr-old pyroclastic deposits and volcanoclastic sediments of the Taupo Pumice Formation (Figure 2; Healy, 1975; Collar, 1985; Wilson, 1993; Browne and Lawless, 2001). Further hot springs ("the lagoon"), fumarolic fields, and collapsed structures within the DOC

thermal area lie in a steam-heated zone northeast of Lake Rotokawa. Many of the DOC thermal features were modified by sulphur mining during the 1960s–1990s (Jury, 1984; Sinclair, 1989; Bardsley and Williams, 2017). Fumaroles, acid–sulphate–chloride, and silica-rich springs are also found in isolated spots along the Parariki Stream (Sriaporn et al., 2020). Northeast of the DOC thermal area, a third zone contains a series of large collapse pits with boiling springs, steaming grounds, and fumarolic vents at Sulphur Cliff (Figure 2).

2) In the northern area, there are fewer thermal features with chloride–bicarbonate springs along the banks of the Waikato River and localised small areas of steaming ground (Browne, 1988; Browne, 1989).

Surficial geology around Lake Rotokawa includes several hydrothermal eruption breccia units, collectively mapped as the Parariki Breccia, and thick sequences (tens of metres) of Holocene tephra fall (e.g., Hinemaiaia, Waimihia, and Mapara tephra) and pyroclastic flow deposits (e.g., Taupo Pumice), mainly sourced from the Taupo Volcano (Collar and Browne, 1985; Browne and Lawless, 2001; Leonard et al., 2010; Milicich et al., 2020b). Below this, the shallow (<400 m) geology consists of a series of ignimbrites (Oruanui ignimbrite), rhyolitic dome deposits (Oruahineawe and Fulljames rhyolites), and volcaniclastic succession (Huka Falls and the Waiora Formation; Milicich et al., 2020a; references therein).

3 Methods

This study applies a combination of field and laboratory methods to analyse the physical and mechanical properties of

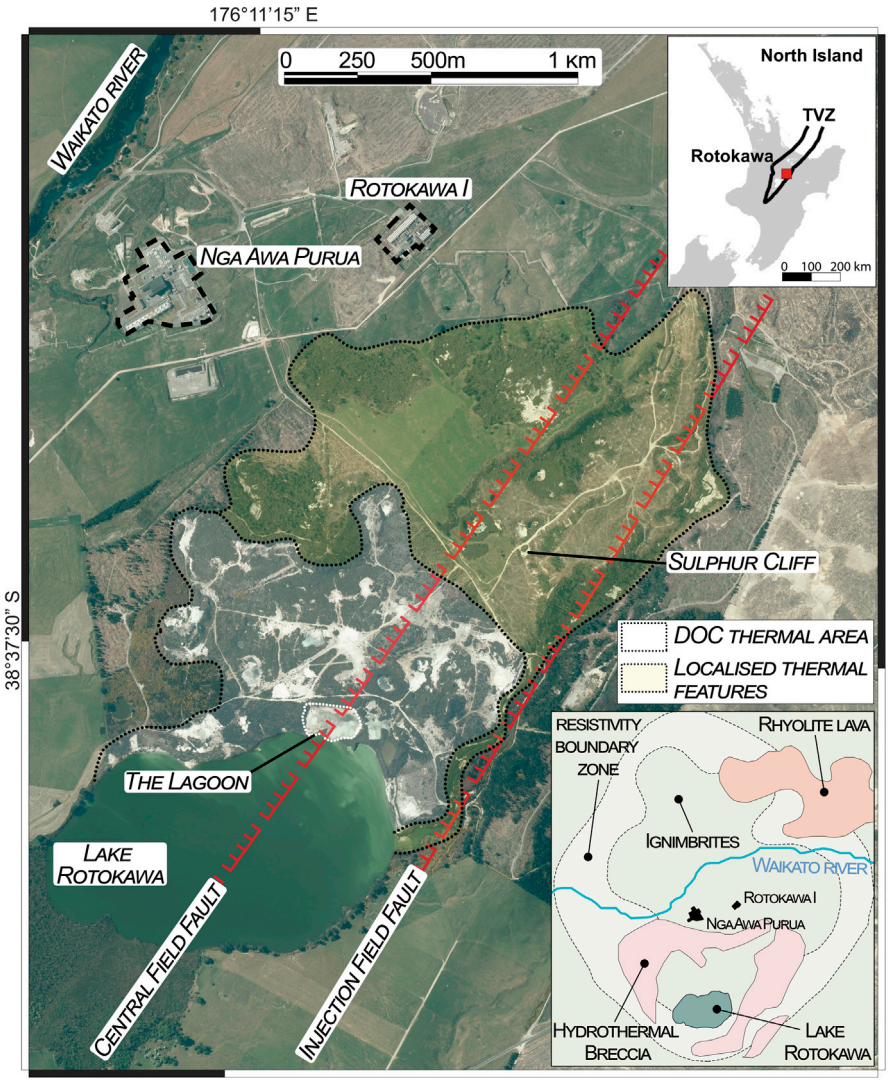

FIGURE 1
Satellite image (Google Earth™, 2016) of the southern sector of the Rotokawa geothermal field and surrounding areas. The Nga Awa Purua and Rotokawa I power stations are located north of a geothermal area characterised by active surficial manifestations. The investigated zones include a highly active and more widespread thermal area, part of the Department of Conservation (DOC) land (highlighted in white), and a thermal ground with localised and/or patched thermal features (highlighted in yellow). The Central and Injection Field Faults and the locations of "the Lagoon" and of "Sulphur Cliff" are shown. In the bottom right inset, a map of the Rotokawa geothermal field with simplified surface geology from Leonard et al. (2010) and the 30 Ωm resistivity boundary zone of Risk (2000) is shown.

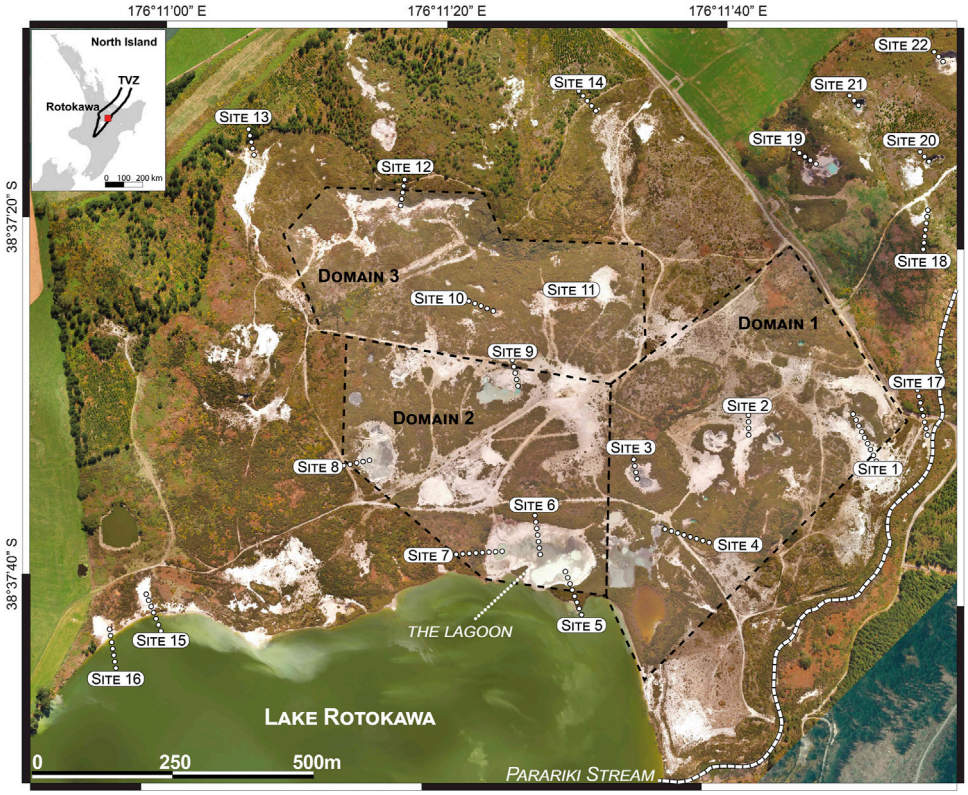

FIGURE 2
LiDAR image of the DOC thermal area and surroundings showing the location of the main geothermal features and the approximate extension of domains 1, 2, and 3. Areas surrounding these features were investigated for subsoil characterisation, measurements of temperatures, and petrophysical properties and for sampling of soil and sinter material for laboratory analyses.

hydrothermally altered soils and hard, sulphur-cemented grounds present within the Rotokawa DOC thermal area. Field methods include mapping the surface geothermal features, describing top and subsoil layers (in pits and natural exposures), and characterisation and sampling areas of hardened lithologies. For each analysed soil layer or hard ground, where possible, we measured temperature, permeability, and shear and compressive strength. Soil layers were also distinguished by the alteration degree defined by their macroscopic features (change of structure, colour, and mineral assemblage). Collected samples were also taken as representative of the soils and hard grounds in the mapped but uncharacterised areas. We also measured the distribution of surficial temperatures (<15 cm). Geothermal feature mapping and temperature measurements were conducted simultaneously and were focused in the central–eastern portions of the DOC thermal area (Figures 2, 3), albeit restricted by vegetation cover and unstable ground. A Trimble Juno 3D handheld GPS device and a 0.5 m-resolution georeferenced drone image were used to locate temperature measurements and soil profiles. Surface features, temperatures, and soil logs were integrated into a GIS to produce digital maps. Laboratory methods included measurements of dry petrophysical properties (density and connected porosity) of consolidated (e.g., hard ground, pumice, and sinters) and unconsolidated samples. Additional definitions, information, and maps related to geothermal feature mapping (3.1) and subsoil and exposed surface profiles (3.2) are reported in the Supplementary Material (SM).

3.1 Geothermal feature mapping

Geothermal manifestations in the DOC thermal area were mapped according to the "*Guideline for mapping and monitoring geothermal features*" (Scott, 2012) and include mixed flowing springs and non-flowing pools; mud pots and pools; superheated and hot fumaroles; and steaming and heated grounds (see details in Supplementary Material 1). We recognised four typical groups that include one or more of these features characterising specific sites of the DOC thermal area (Figures 2–6), and those can be divided as follows:

Spring and pools comprise mixed flowing springs and pools of both turbid or milky waters, as well as mud pots and pools of muddy waters and/or mud dominated. The rims and outflows of pools are covered in silica sinter deposits. Sulphur-cemented ground is defined as areas where surficial decimetre-thick sandy subsoils are cemented by native sulphur. These may be over large areas or form isolated patches. Fumaroles and steaming and heated grounds are areas with intense degassing and warm ground likely associated with subsurface fractures. Unstable ground and collapse structures include areas characterised by unsafe and subsiding soils in the proximity of

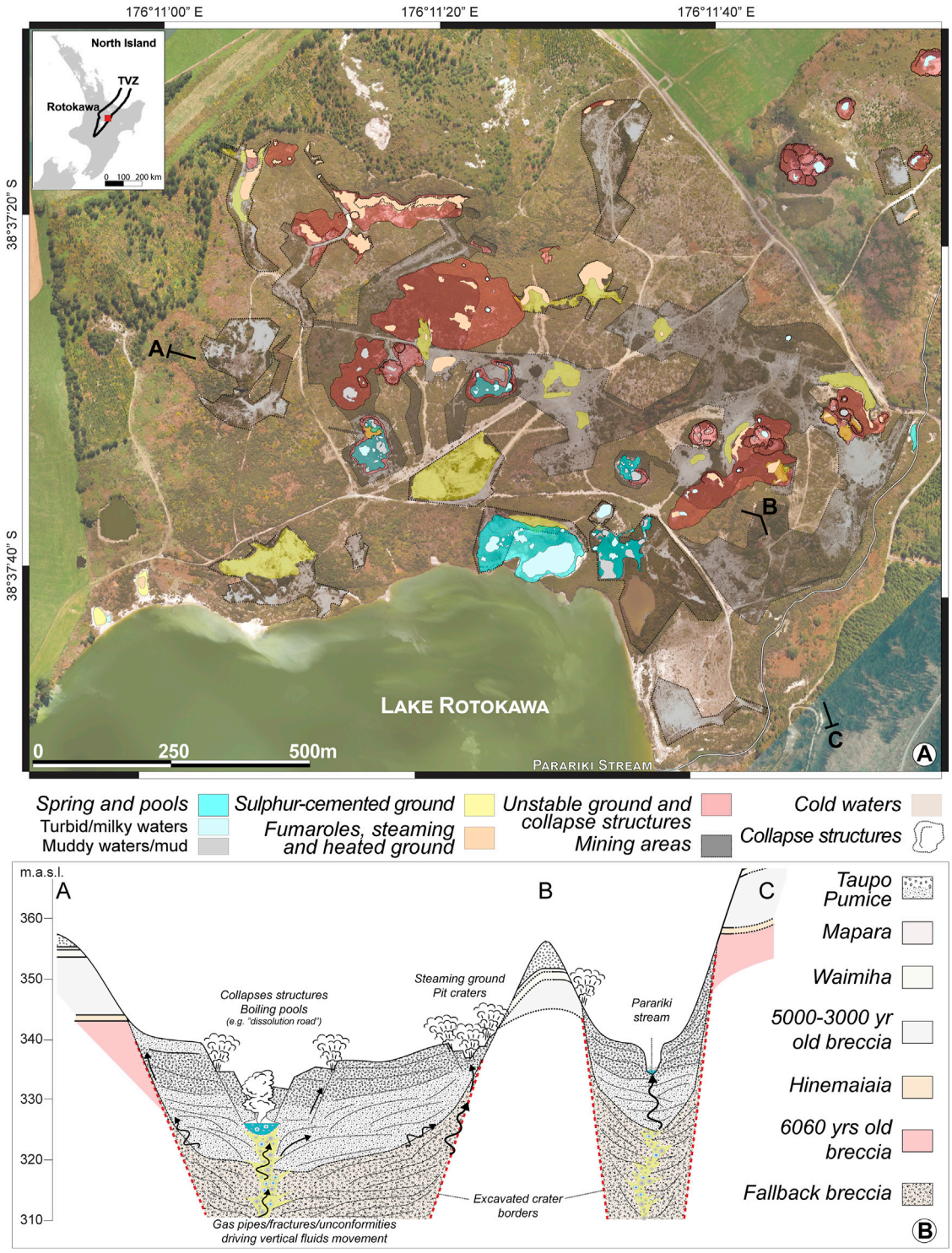

FIGURE 3
Map of geothermal features and shallow geologic settings. **(A)** LiDAR image of the DOC thermal area and surroundings, showing the distribution of main geothermal features (each site is indicated with a colour associated with the main geothermal feature group), mining areas, basins with cold waters, and collapse structures. *In situ* characterisation in the mapped areas included permeability (m^2) of soil levels, as well as temperature (°C) and strength (kN/m^2) profiles (stratigraphic logs and measured properties of representative profiles are shown in Figures 8–10). The dashed line represents the profile of the conceptual cross section shown in b. **(B)** Schematic cross-section (x10 vertical exaggeration) shows the outcropping lithological units around the DOC thermal area and the shallow fluid flows expected within the Taupo Pumice and breccia fallback deposits.

highly degassing zones and/or collapsing structures. Generally, the ground can consist of reworked material mounds, fractured bedrocks, and *in situ* geological units strongly leached by rising and acidic fluids.

In addition to these groups of thermal manifestations, we included excavated areas that were delimited by using historical orthophotos and maps from the last 70 years, during which

significant mining efforts took place (Bardsley and Williams, 2017).

3.2 Subsoil and exposed surface profiles

Two types of soil profiles were measured: those dug in the ground for subsoil characterisation and the exposed surface around fumaroles and/or steaming spots (Supplementary Figure S1A). For the investigated profiles, we carried out measurements of petrophysical properties of the main soil types (Figures 7–10) and sampled some soil materials for laboratory analyses. Due to their abundance in subsoils and their highly porous nature, pumices likely played a key role in controlling the permeability of fluids around the DOC thermal area. Therefore, we also measured the *in situ* permeabilities of unaltered and altered pumice clasts from primary and reworked hard grounds and soils. As well, we collected pumice samples from representative sites for determining their densities and porosities in the laboratory (Supplementary Tables S1, S2).

3.2.1 Field-based methods

Measurements of permeability of unconsolidated material representative of subsoil types and hard ground at the DOC thermal area were taken using a PL-300 soil permeameter and a portable air permeameter (Supplementary Material 2, 3 and Supplementary Figure S2; Umwelt-Geräte-Technik 2012; Heap et al., 2017; Mayer et al., 2017; Montanaro et al., 2017; Rott et al., 2019). For some of the investigated sites, the permeability of soils or hard ground could not be measured because of the increased pore humidity and/or temperature. A total of 83 soil strength measurements and 53 soil permeability measurements were collected from 25 subsurface soil profiles (Figures 8–10 and Table 1). Moreover, 197 measures of permeability were taken from hard grounds (Supplementary Table S1). Cylinders of known volume were used to collect samples for laboratory investigations and were weighed to determine bulk density. This technique allowed the preservation of sample texture and water content. Soil strength was determined by a pocket penetrometer (Zimbone et al., 1996) and a torvain (Farquhar et al., 2001), giving unconfined compressive and undrained shear strengths, respectively (Supplementary Figure S2).

All measured petrophysical and mechanical properties were well within the range of the applied instruments. Field methods are often not comparable in terms of the standard error of measurement with well-constrained laboratory methods (Heap et al., 2017); however, they are internally consistent.

3.2.2 Laboratory-based methods

Soil samples, sinters, sulphur-cemented crusts, and pumices were further characterised in the laboratory to determine their petrophysical properties (Supplementary Table S2). Selected sinter and crust samples were cored perpendicular to layering, if present, and selected pumice samples were cored parallel to the long axis of the elongated vesicles in the pumice. Samples were dried in an oven at 65°C for at least 24 h until fully dry. Weighing of samples before and post drying allowed determination of their water content. The dry powder density of all samples was obtained by a helium pycnometer (Ultrapyc 1200e®, Quantachrome). Knowing the volume of the sampling cylinder, as well as the water content and dry density, allowed the determination of the porosity of the samples, which is a key parameter controlling their mechanical behaviour (Pola et al., 2014; Heap et al., 2015).

3.3 Temperature measurements

Soil temperatures were measured using a digital thermocouple (0.01°C accuracy) inserted approximately 15 cm within the ground surface, within the depth range where air temperature can play a role in the soil temperature (Brown et al., 2000). Air temperatures never remained below 20°C during the field mapping. In areas with thick hard ground, a rock hammer was used to break through and reach an appropriate measurement depth.

Generally, temperatures were measured in transects with a spacing of approximately 5 m. In colder areas with little temperature variation between measuring points, spacing was increased to approximately 10 m. In areas with higher temperature variation (>10°C), measurement spacing was decreased to as little as 0.5 m to efficiently capture local temperature variation. In areas with fumaroles and/or steaming features, the measurement grid was adjusted to determine the extent of surface heating.

Water temperatures of springs and pools were measured using a wired thermocouple (0.01°C accuracy) fully submerged in water. In case of large pools, we tried to get the thermocouple as close as possible to the bubbling vent area to obtain the most representative possible water temperature values.

4 Results

4.1 Morphology of the DOC thermal area and surroundings

The overall morphology of the investigated area results from a combination of eruption craters filled by the Taupo pumice deposit, later modified by mining excavation (Supplementary Figure S1B). In general, the DOC thermal area shows i) a flat area at 335–336 m above sea level (a.s.l.) that extends 100–400 m north of the lake shoreline, connected by gentle to steep slopes to ii) a series of terraces ranging in elevation between 339 and 345 m, and iii) a gently sloped ground rising to 353.5 m, which connects terraces to the steep eruption crater rims (elevation up to 360–400 m). A localised 360-m-high mound is located between domain 1 and the Parariki Stream. Most of the features in the W and SW portions of domain 1 (e.g., sites 3 and 4) and the depressions in domain 2 have been excavated down to a depth of 335 m. As well, many of the naturally collapsed structures in domains 1 and 2 and at sites 19–22 have their bottom filled by springs at the water table level of ~334.5–335 m.

4.2 Surficial features of the DOC thermal area and surroundings

Detailed mapping and *in situ* analysis allowed us to distinguish three main spatial domains based on the prevalent groups of geothermal features, soil types, and the apparent differences in alteration, namely, domains 1, 2, and 3 (Figures 2, 3). Domain 1 with numerous and closely spaced collapsing structures and springs/pools is located in the eastern terraced part of the DOC

10.3389/feart.2022.1067012

FIGURE 4
Main geothermal features in domain 1. **(A, B)** Typical collapsed structures and sulphur-cemented grounds around site 1. **(C, D)** Collapsed structures and sulphur-cemented grounds around site 2. **(E)** Springs, mud pools, and fumaroles in the Middle Earth (site 3). **(F, G)** Springs and mud pools within site 4.

thermal area (sites 1–4). Domain 2 is located in the central field, around the flat area surrounding the lake, which includes three large depressions with a large variety of springs and pools (sites 5–9). Domain 3 is located in the northern portions of the DOC thermal area, over the gently sloped ground connecting terraces to the eruption crater rims, where degassing features and sulphur-cemented and unstable grounds dominate the landscape (sites 10–12). All of these domains developed within areas of intense mining and are separated and/or surrounded by zones with sulphur-encrusted ground, reworked material, and abundant vegetation.

10.3389/feart.2022.1067012

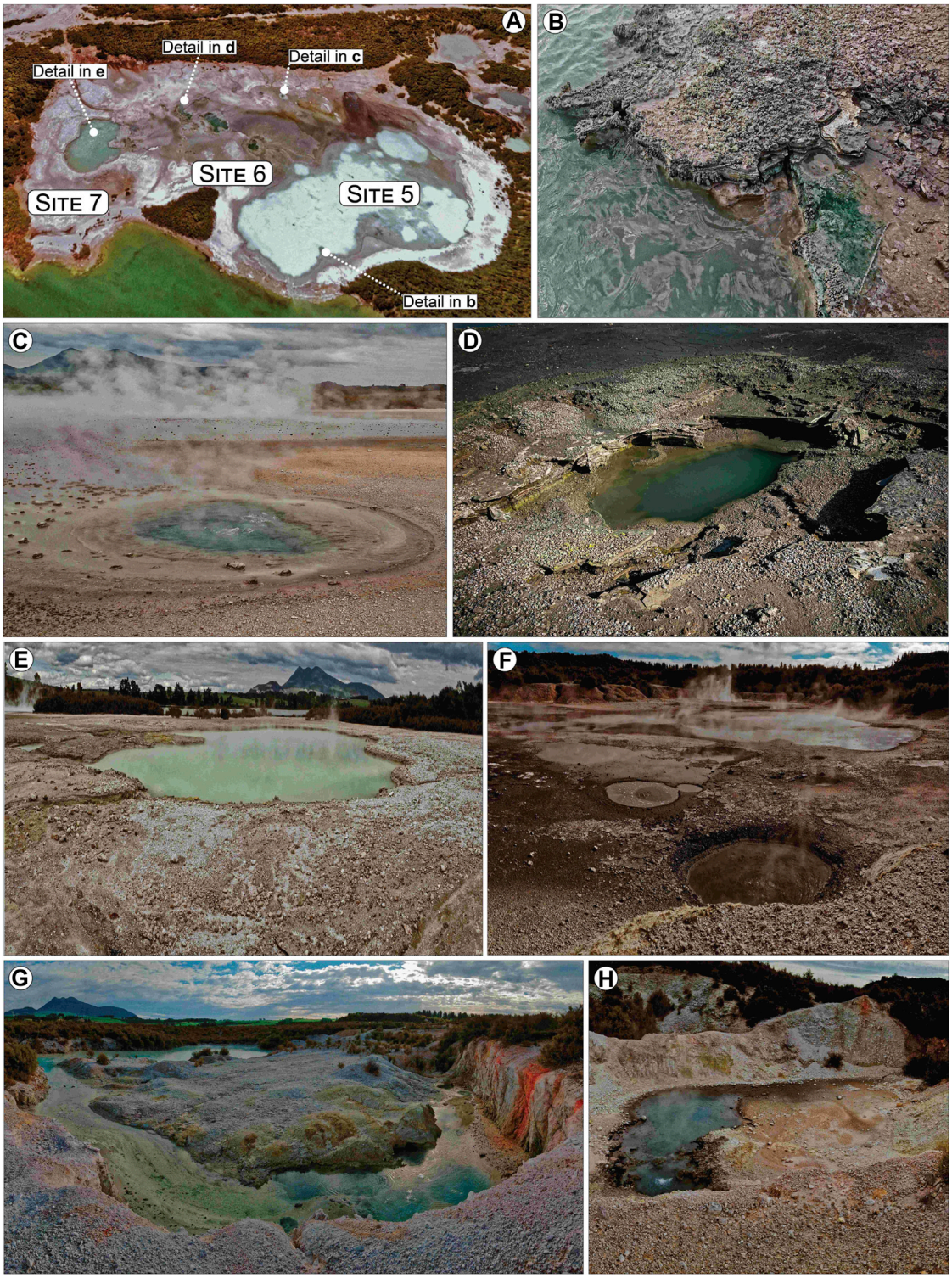

FIGURE 5
Main geothermal features in domain 2. **(A)** Aerial view of the Lagoon showing the location of sites 4–7. **(B–E)** Details of the sinter-type deposit in the Lagoon varying from stromatolitic deposits **(B, C)** to fine-grained, laminated silica sinters **(D, E)**. **(F)** Examples of mud pots and pools with associated deposits at site 8. **(G, H)** Mined areas with reworked material mounds and surfacing springs around site 9. Patchy sulphur-cemented and highly altered areas can be recognised.

Small areas with geothermal features can also be found in the northern (sites 13 and 14), western (sites 15 and 16), eastern (site 17), and northeast (sites 18–22) sides of the DOC thermal area.

All the described areas and features are shown in Figures 3–6, as well as reported in detailed maps within the Supplementary Material (Supplementary Figures S3–S5).

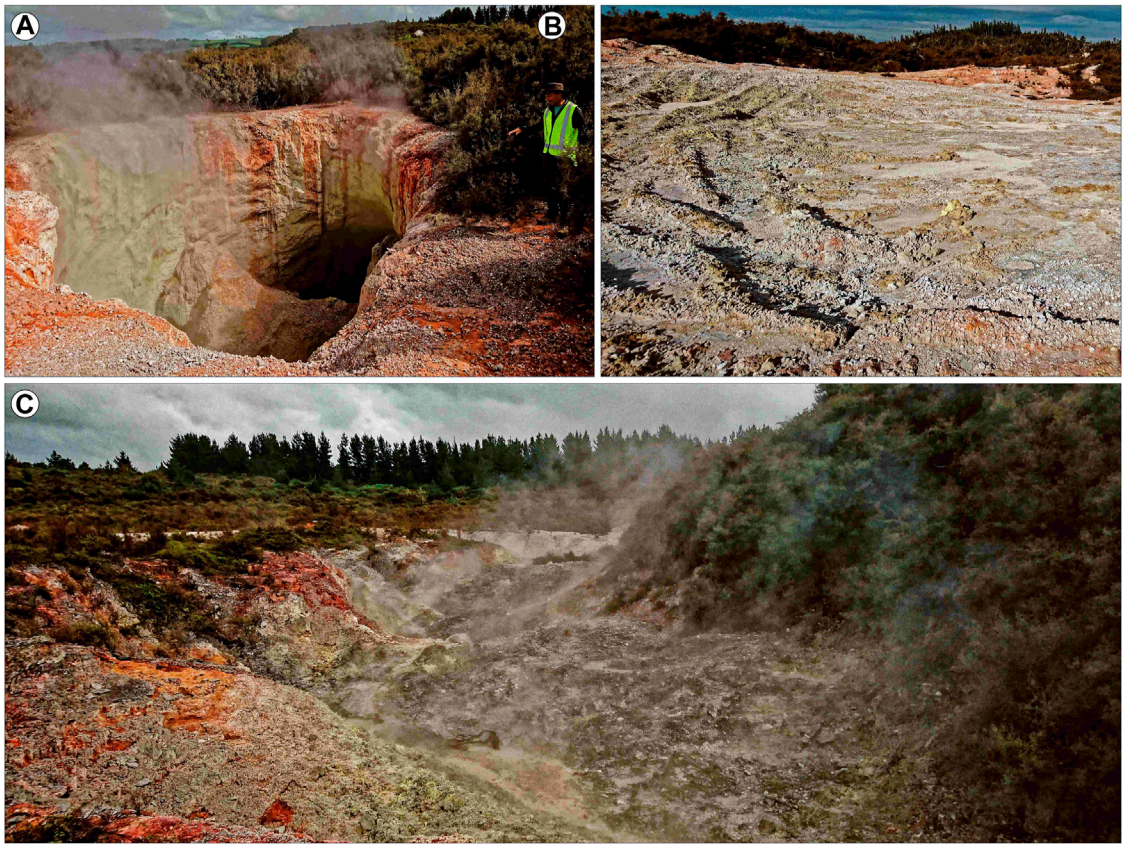

FIGURE 6
Main geothermal features in domain 3. **(A)** Detailed view of the Rainbow crater at site 10. **(B)** Sulphur-cemented tread tracks at site 11. **(C)** Highly degassing dissolution structures and a collapsed pit at site 12. On the left and in the central part of the depression, altered soil made of the Taupo Pumice deposit. On the right side, vegetation is covering the altered breccia deposit.

4.2.1 Domain 1

Domain 1 occupies most of the eastern sectors of the DOC thermal area, and the surficial expressions are aligned along a NE–SW axis (Figures 2, 3 and Supplementary Figure S3). In the central and northeastern portions of the domain (sites 1 and 2), there are abundant natural collapse structures with and without springs and pools at their base. Springs and pools are mostly milky to turbid in colour, with mild to intense bubbling and steaming activity. Collapse pits can be isolated with a 10–30 m maximum diameter or form coalesced structures up to 45 m wide (Figures 4A–C). From NE to SW, the depth of these structures decreases from ~10 to ~6 m. Other typical features surrounding the collapse structures and often-occupying excavated areas include sulphur-cemented, steaming and heated grounds with spotted fumaroles (Figures 4B, D). Unstable grounds, consisting of altered, reworked, or *in situ* material, are normally found in areas between collapse structures. In the southwest portions of the domain (sites 3 and 4), the presence of springs and pools of different compositions characterises depressed areas produced by mining activity (Figures 4E–G). Site 3 is one of the most spectacular geothermal manifestations, informally known as "Middle Earth." Here, a variety of bubbling milky-to-green waters and blackish mud pools, sulphur-rich deposits, fumaroles, and intensively degassing pools are found within a 50×30-m-wide area (Figure 4E). Site 4, in the south-western part of domain 1 (Figures 4F, G), contains a range of water springs mixed with muddy pools, within a rectangular area.

4.2.2 Domain 2

Domain 2 is located in the central sector of the DOC thermal area (Figure 2; Figure 3; Figure 5A and Supplementary Figure S4) and includes five main sites: sites 5–7 are located within a ~180×110-m-large, ~E–W directed, depressed area dominated by mixed water springs and pools, known as the Lagoon; site 8 corresponds to a ~N–S elongated, ~100×60-m depression showing a mixture of water springs and abundant mud pools; and site 9 consists of a series of ~10×10 m–~80×70 m large depressions containing a mixture of water springs. All depressions are located within partially or extensively excavated areas related to the mining phase.

Springs and pools in site 5 form almost continuous coalesced structures, ~100 m long and directed NE–SW, and are mostly milky in colour, showing mild to intense bubbling and steaming activity (Figure 5A). Microbial mats and stromatolites are present at several localities around these hot pools (Figure 5B). Muddy and laminated sinter deposits, with localised hot water springs and stromatolites (Figures 5C, D), dominate site 6. The springs at site 7 include isolated pools 3–30 m wide with turbid waters showing mild bubbling (Figure 5E). The surface outflow area of all springs and pools, marked by a strandline of pumice pebbles, is characterised by the presence of various sinter deposits.

The depression at site 8 is filled with a variety of bubbling milky waters on its western side and bubbling mud pools on its eastern and north sides (Figure 5F). Sulphur-cemented ground can be found in the

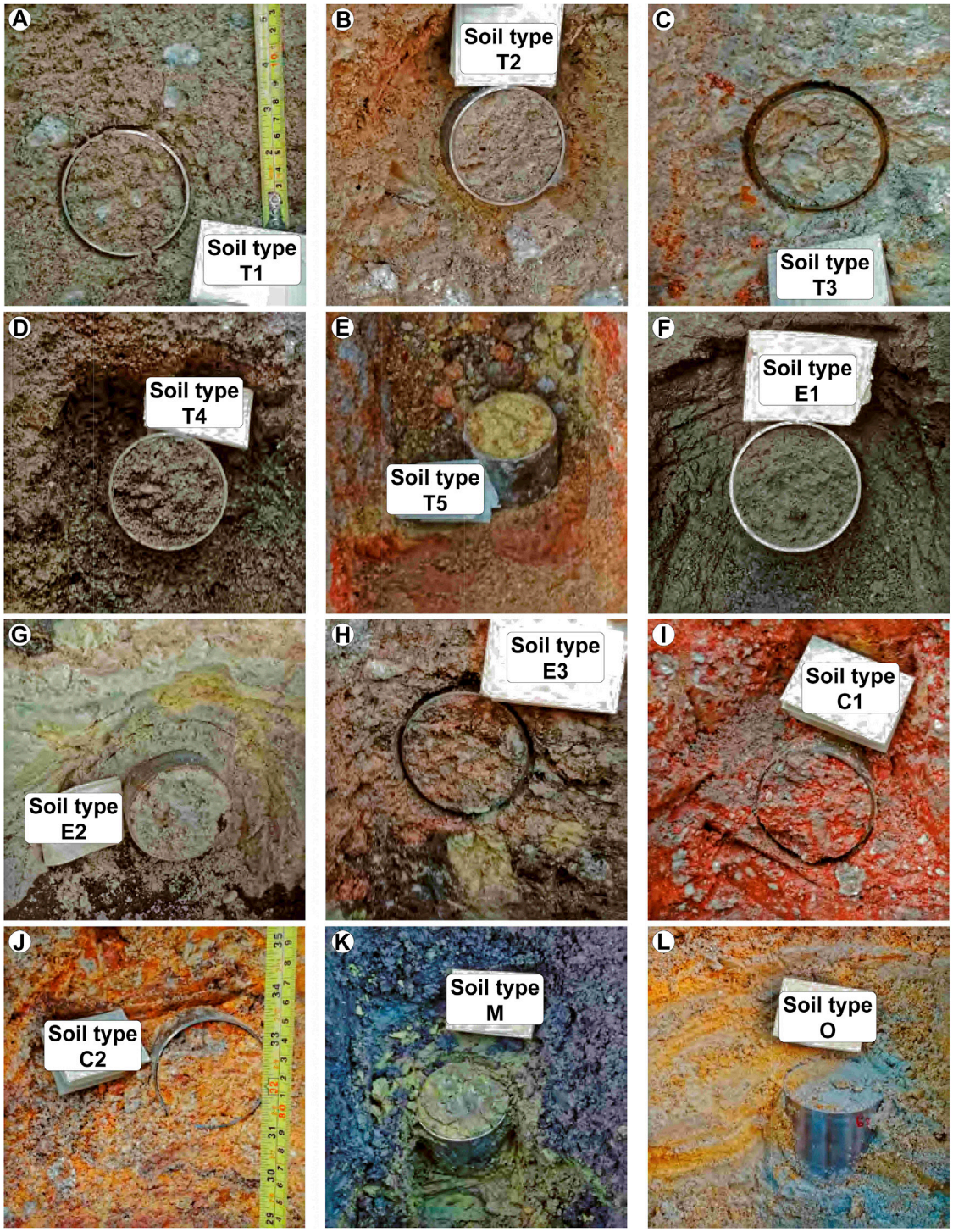

FIGURE 7
Main subsoil layer types. **(A)** Unaltered or weakly altered Taupo Pumice fine-grained layers (T1). **(B)** Moderately altered Taupo Pumice fine-grained layers (T2). **(C)** Strongly altered Taupo Pumice fine-grained layers (T3). **(D)** Weak to moderately sulphur-altered Taupo Pumice coarse-grained layers (T4). **(E)** Highly sulphur-altered Taupo Pumice coarse-grained layers (T5). **(F)** Sand to very fine gravel dark grey layers (E1). **(G)** Silty grey to white layers (E2). **(H)** Sandy dark to light pink and brown layers (E3). **(I)** Dark red clayey layers (C1). **(J)** Variegated clayey layers (C2). **(K)** Layers rich in clay commonly found in excavated and depressed areas with mud pools (M). **(L)** Variegated silty and sandy layers crossed by roots and show clear signs of oxidation (O).

northern portion, while most of the pools are surrounded by unstable ground and locally by collapsing structures. A zone between the two large depressions is characterised by the presence of a patchy sulphur-cemented and cold ground (Supplementary Figure S4).

The area around site 9 includes a variety of natural and mining-related features, with emergent water springs and/or mud pools, as well as overimposed natural collapsed structures (Figures 5G, H, and Supplementary Figure S4). In particular, the largest depression in site

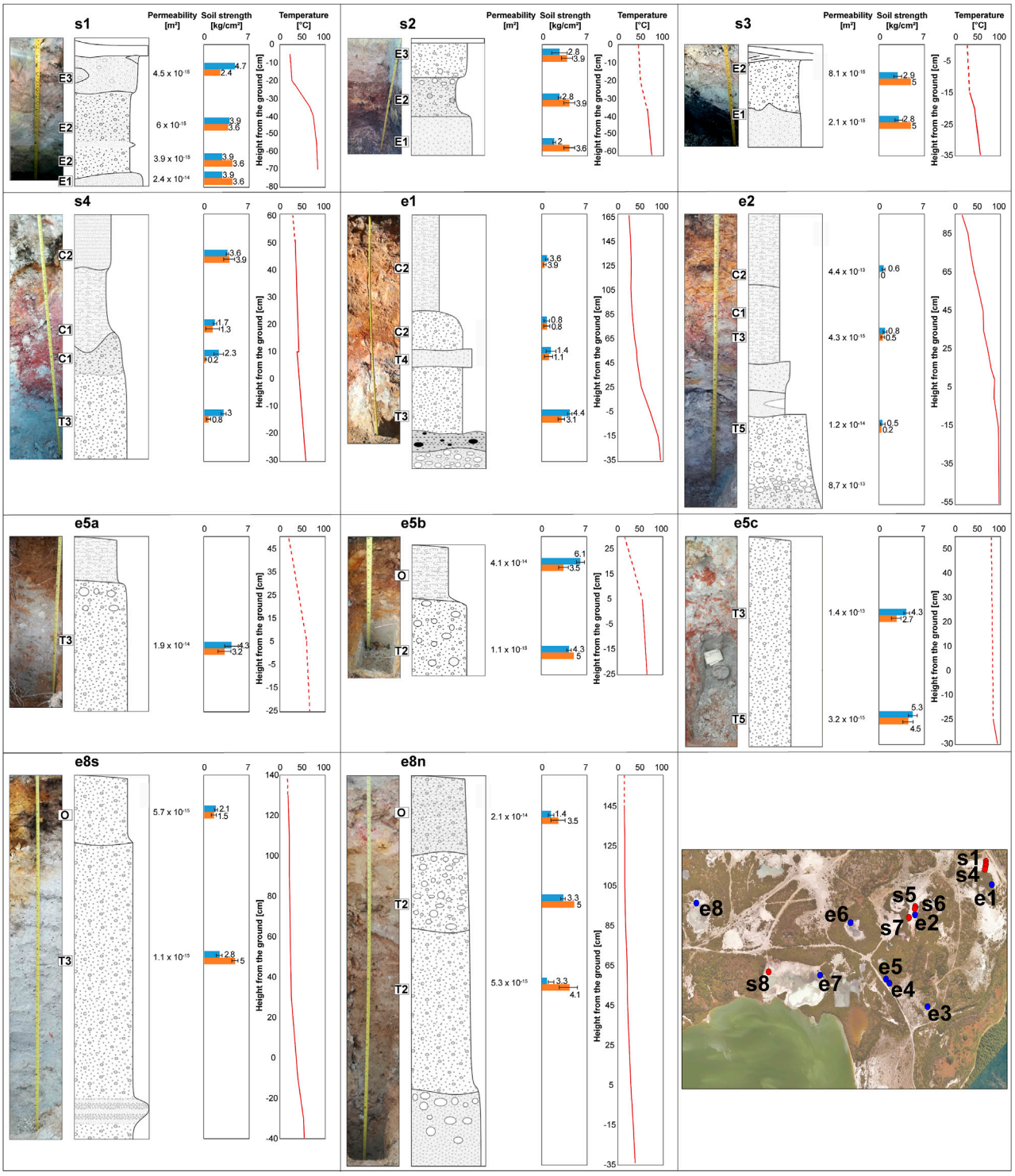

FIGURE 8
Subsoil and exposed profiles in domains 1 and 2. Permeability, compressive (blue bar) and shear (orange bar) strength, and temperature profiles are reported for each soil layer and exposed profile. The missing spot properties are listed in Table 1.

9 contains mostly milky-coloured water, with a couple of turbid water springs, all showing mild to intense bubbling (Figure 5G). The other depressions show mostly turbid to muddy waters, with mild to intense bubbling activity accompanied by weak degassing (Figure 5H). Unstable ground characterised the rim and inside the walls of these excavated areas, while heated grounds and sulphur cementation had developed on tread tracks and were locally present on the rim and surrounding areas.

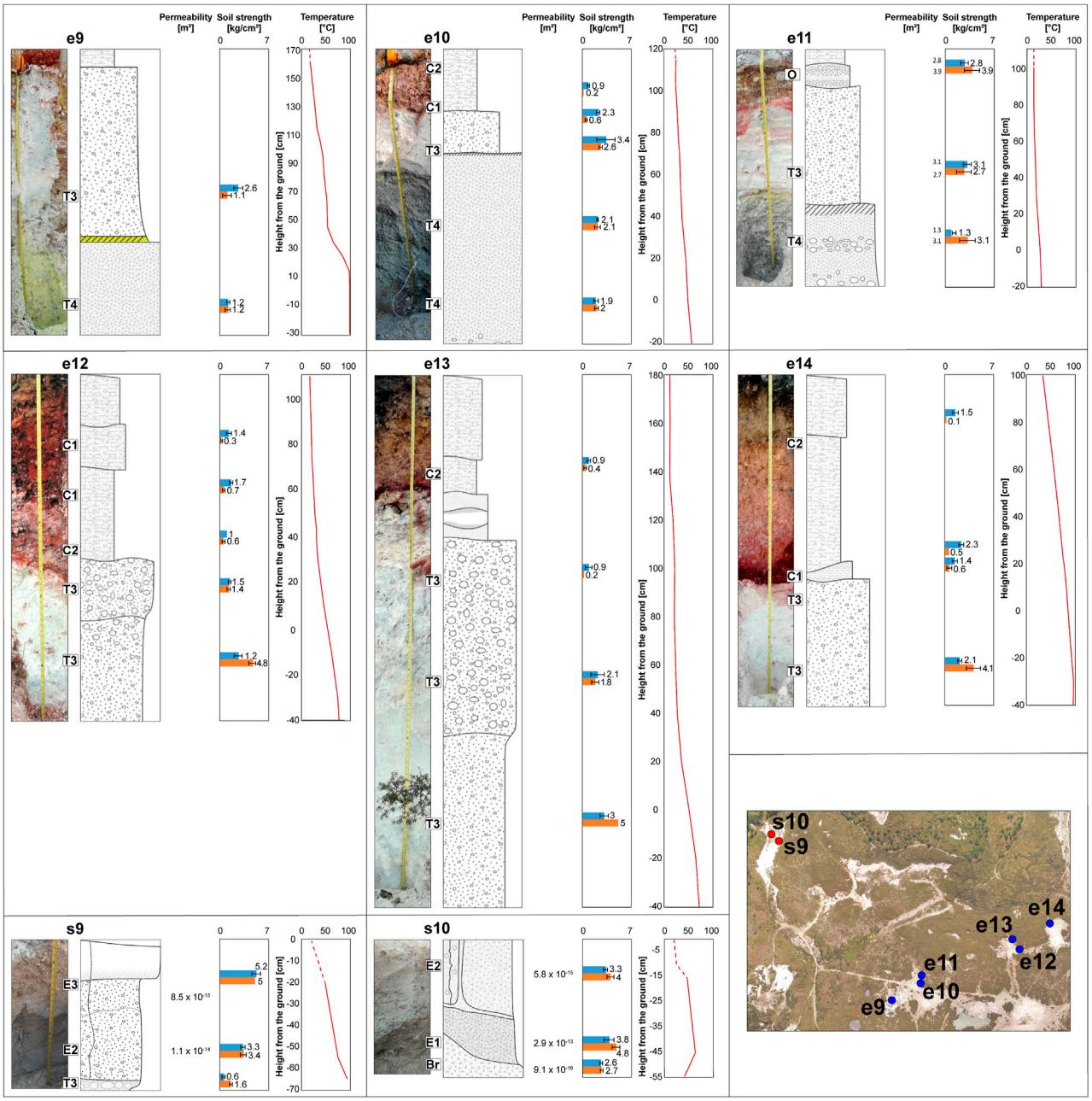

FIGURE 9
Subsoil and exposed profiles in domain 3. Permeability, compressive (blue bar) and shear (orange bar) strength, and temperature profiles are reported for each soil layer and exposed profile. The missing spot properties are listed in Table 1.

4.2.3 Domain 3

Domain 3 occupies the northern sector of the DOC thermal area (Figures 2, 3 and Supplementary Figure S5) and includes site 10, characterised by scattered depressions and collapse pits, varying in size from ~10×10 m to ~20×40 m; site 11, comprising two shallow excavated sites from ~35×40 m to ~40×60 m large; site 12 is a ~200-m-long and ~10-m-wide depression, W–E oriented. Many of the features overlap or develop within mined areas.

In site 10, degassing depressions and collapsed structures surrounded by unstable ground occur with or without bubbling pools (Figure 6A). Site 11 is mostly dominated by sulphur-cemented ground developed on tread tracks, with localised fumaroles and steaming and heated ground (Figure 6B). Site 12 is one of the hottest features in the whole DOC thermal area and is dominated by highly altered, friable, and unstable ground with collapsing rims. The fissure is located at a geological contact—likely a crater rim—between the Taupo Pumice deposit and a bedrock made of Oruanui ignimbrite and Pararaki breccia deposits (Figure 6C). At the west end of the fissure, there are excavated areas with unstable grounds and a ~10 m large collapsed pit, as well as fumaroles and steaming and heated ground (Supplementary Figure S5).

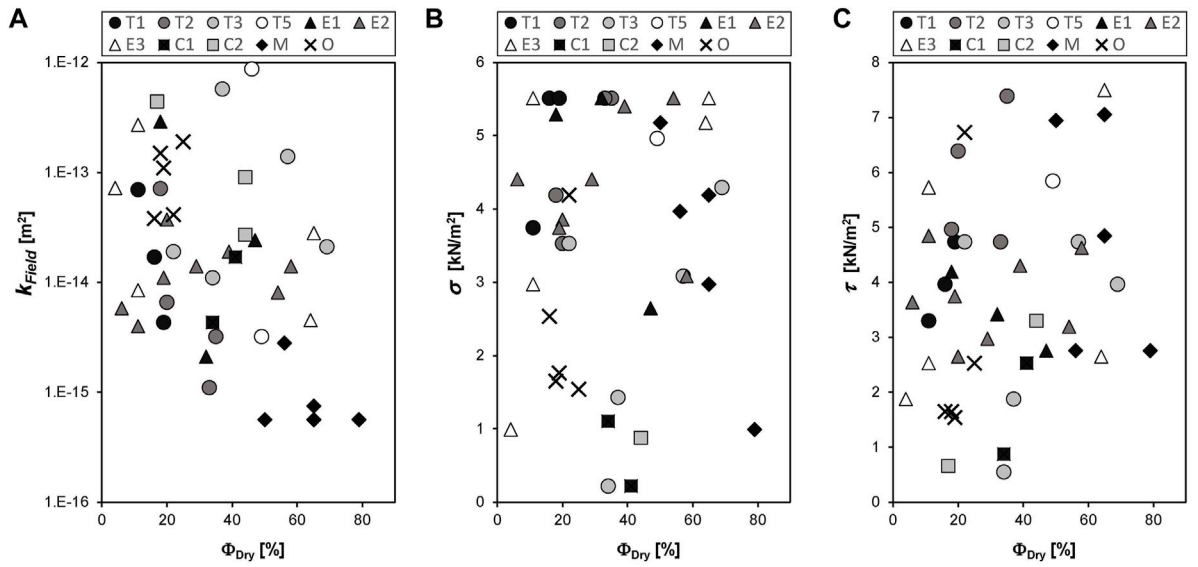

FIGURE 10
Permeability **(A)**, normal **(B)** and shear strength **(C)** in relation to the connected porosity of soil layers measured at Rotokawa's DOC thermal area. Permeability values were measured in the field using TinyPerm III.

4.2.4 Thermal features outside the main domains

North of the DOC thermal area, within one excavated area at site 13, we found dominant sulphur-cemented and heated grounds surrounding the unstable and degassing areas (Supplementary Figure S6A). Adjacent to this, there is a ~50×60 m large area with unstable ground and collapsed pits 5–10 m wide, as well as a small excavated zone with degassing pits (Figure 3A). In the northern end of the DOC thermal area, at site 14, a ~6×60 m large section is characterised by small fumaroles, degassing, and heated, unstable ground (Supplementary Figure S6B). Along the western lakeshore at sites 15 and 16, respectively, we found patches of sulphur-bearing pumice clasts and slightly heated ground, as well as water springs showing weak bubbling (Supplementary Figure S6C). At site 17, siliceous stromatolitic sinters are formed in acid–sulphate–chloride spring outflows (Supplementary Figure S6D; see also Schinteie et al., 2007). Along the Pararíki Stream, several other spots are characterised by active degassing with mild to intense bubbling in the water (Figure 2, and Supplementary Figure S6E).

In the NE sector outside the DOC thermal area, within the excavated site 18, there is a large fumarole (at Sulphur Cliff) that is altering a substrate of Oruanui ignimbrite and breccia deposits (Supplementary Figure S6F). In the same sector, there is a series of ~30×40 m–~70×90 m large and ~20-m-deep collapsed structures (sites 19–22) all containing milky waters showing intense bubbling and accompanied by vigorous steaming (Supplementary Figures S6G, H).

4.3 Unconsolidated subsoil types

4.3.1 Top and subsoil layers and their distribution

Soil layers were categorised as undisturbed vs. reworked and unaltered and altered, as well as depending on their granulometry and average petrophysical and mechanical properties (Figures 7–10; Table 1). The first group includes soil layers within the *in situ* Taupo Pumice deposits (T) and generally shows no obvious reworking or mechanical disturbances to the original textures, though their degree of chemical alteration is variable. The main layer types are as follows:

Unaltered or weakly altered Taupo Pumice fine-grained layers (T1). These layers show a light grey to light brown, silt to sand-sized matrix, supporting granule- to boulder-sized pumice (Figure 7A). Layers T1 can vary from matrix to clast-dominated, show a low permeability (4.3×10^{-15} to 1.7×10^{-14} m²) and low porosity (11%–19%), are hard in consistency (3.7–5.5 kg/cm²), and have a high shear strength (3.3–5.5 kg/cm²).

Moderately altered Taupo Pumice fine-grained layers (T2). In this layer, the primary clasts, matrix, and original colour are recognisable. The matrix is light to brown orange and consists of silt to sand-sized materials, supporting granule- to boulder-sized pumice clasts (Figure 7B). Pumice-rich parts are generally altered, but their texture is still recognisable. Layers T2 have low permeability (1.1×10^{-15} to 7.1×10^{-14} m²), low-to-medium porosity (18%–33%), is very stiff to hard in consistency (3.5–5.5 kg/cm²), and have a low to very high shear strength (1.5–7.4 kg/cm²).

Strongly altered Taupo Pumice fine-grained layers (T3). Such layers have a white to grey matrix dominated by silt and clay-sized particles, with a minor sand component. Portions rich in pumiceous granule- to cobble-sized clasts show stronger alteration and are much weaker than matrix-rich variants. Pumices may be altered to the point where their texture becomes entirely unrecognisable (Figure 7C). Layers T3 show a low to high matrix permeability (1.1×10^{-15} to 1.4×10^{-13} m²), medium-to-high porosity (22%–69%), a highly variable consistency ranging from very soft to hard (0.2–5.5 kg/cm²), and have a low to very high shear strength (0.6–4.7 kg/cm²). It is to be noted that the very soft to firm layers (σ<1 kg/cm²) have a double value of shear strength (up to 1.5 kg/cm²).

Weak to moderately sulphur-altered Taupo Pumice coarse-grained layers (T4). These layers are dark grey, pebble- and cobble-rich soils with abundant centimetre-sized sulphur nodules and sulphur

crystals <0.5 mm in size (Figure 7D). Such layers generally show a clast-supported texture and develop within coarse layers of the Taupo Pumice deposits in warm areas proximal to degassing sites, where measurable layers T4 show high permeability (2.9×10^{-13} m^2), low porosity (18%), are stiff to hard in consistency (1.2–5.3 kg/cm^2), and have a low to medium shear strength (1.3–4.2 kg/cm^2).

Highly sulphur-altered Taupo Pumice coarse-grained layers (T5). These layers are yellow-stained and rich in sulphur mineralisation. The original lithology is often disrupted, though a coarse-grained texture could be recognised, and sulphur is distributed throughout the layer as crystals or nodules less than a few centimetres in size (Figure 7E). Layer T5 occurs nearby (<1 m) to active degassing features, shows low to high permeability (3.2×10^{-15} to 8.7×10^{-13} m^2), low porosity (18%), is firm to hard in consistency (1–5 kg/cm^2), and has a low to medium shear strength (1.9–5.8 kg/cm^2).

The second group of soil layers is typical of areas that have been excavated for mining (E) and includes mostly reworked materials. These layers may be similar in granulometry and component to the Taupo Pumice type, but the original deposit texture and geometry have been disrupted, and the material has been reworked and/or compacted. This layer group comprises

Sand to very fine gravel dark grey layers (E1). These layers generally are dominated by sandy material and contain <10% pumice with sizes <2 cm (Figure 7F). They can only be found in the excavated area on the eastern side of the DOC thermal area (location of s1—s4 and e1 at site 1; Supplementary Figure S1A). Layers E1 show a very low-to-low permeability (<5.6×10^{-16} to 2.4×10^{-14} m^2), a medium porosity (32%–47%), a varying consistency from very stiff to hard (2.2–5.5 kg/cm^2), and a low-to-medium shear strength (2.2–3.4 kg/cm^2).

Silty grey to white layers (E2). Such layers are dominated by a silty matrix and a minor sandy component, with <15% of pumice granule (<3 cm) and sporadic pebble-sized clasts (up to ~6 cm; Figure 7G). Layers E2 are similar in appearance to T3, but show a lower permeability (4×10^{-15} to 3.7×10^{-14} m^2), a lower porosity (6%–58%), a harder consistency (3–5.5 kg/cm^2), and a higher shear strength (2.6–4.8 kg/cm^2).

Sandy dark to light pink and brown layers (E3). These layers are very heterogeneous, with significant horizontal variation in texture and physical properties. Pumice content is <30%, with clasts commonly being in the granule to pebble size range (up to ~5 cm). Brown to dark brown soil lenses and large sulphur-mineralised pumiceous clasts are common (Figure 7H). In the E3 layers, only the properties of more consistent layers were measurable, while very friable lenses were too hot and highly degassing for measuring any reliable value. The measured lenses show low-to-moderate permeability (4.5×10^{-15} to 2.7×10^{-13} m^2), low-to-high porosity (11%–65%), very stiff to hard consistency (2.6–7.5 kg/cm^2), and low-to-very high shear strength (2.6–7.5 kg/cm^2).

The third group includes layers made of clay-rich reworked and highly altered material (C), which typically lies between the undisturbed Taupo Pumice and reworked material *via* sharp contacts. Such layers are found in warm areas and in proximity to degassing features. This group includes the following:

Dark red clayey layers (C1). Fine matrix and embedded pumices are generally altered to clay (Figure 7I). The pumice content can vary from absent to up to 30%, with sizes typically in the range of granules to pebbles (<5 cm). These layers show low permeability (4.3×10^{-15} to 1.7×10^{-14} m^2), medium porosity (34%–41%), very soft to stiff consistency (0.2–1.1 kg/cm^2), and low shear strength (0.9–2.5 kg/cm^2). Similar to T3, C1 material has a shear resistance higher than its normal strength.

Variegated clayey layers (C2). This type of soil layer includes a clay-rich matrix exhibiting orange, purple, and red colours within irregular, streaked patterns (Figure 7J). Altered pumices are a major component (up to 50%), with mainly granule- to pebble-sized clasts (up to 8 cm in diameter). These layers show low-to-medium permeability (2.7×10^{-14} to 4.4×10^{-13} m^2), low-to-medium porosity (17%–44%), variable consistency ranging from very soft to stiff (0.1–1.5 kg/cm^2), and low shear strength (0.9–3.3 kg/cm^2). C2 also shows a higher shear resistance than its normal strength.

The fourth group is characterised by variegated silty and sandy layers crossed by roots and shows clear signs of oxidation (O). Minor pumices (<5%) of fine pebble to coarse sand size (<1 cm) occur in the soil matrix (Figure 7K). Layer O is present near or at the ground surface in apparently undisturbed areas, with no geothermal manifestations. This layer shows low-to-high permeability (5.7×10^{-15} to 1.9×10^{-13} m^2), low porosity (16%–22%), stiff to hard consistency (1.5–4.2 kg/cm^2), and low-to-high shear strength (1.5–6.7 kg/cm^2).

The fifth group consists of layers rich in clay commonly found in excavated and depressed areas with mud pools (M). These layers can be laminated and show alternation of beds of clay and very fine sand, with a high water content (Figure 7L). They show a very low permeability (<5.6×10^{-16} to 2.8×10^{-15} m^2), high porosity (50%–59%), and are stiff to hard in consistency (1–5.2 kg/cm^2), with low to very high shear strength (2.8–7.1 kg/cm^2). As for other clay/silt-rich layers, the M layer shows a high shear resistance.

The sixth group is characterised by a light brown brecciated layer (Br). This layer develops over a breccia deposit found in the excavated area at site 13, with granule- to cobble-sized tuffs and lithics embedded in a sandy matrix that appear generally indurated by alteration. At a representative measured spot, layer Br shows very low permeability (9.4×10^{-16} m^2) and low porosity (21%), with a very stiff consistency (3 kg/cm^2) and low shear strength (2.9 kg/cm^2).

4.3.2 Soil distribution

In the central and northeast excavated areas of domain 1, subsoils are mostly developed in the Taupo Pumice deposits (s1—s7 and e1 and e2 in Figure 8 and Table 1). Soil layers of the first group can be found with different alteration states (T1–T5), with more altered layers closer to or in correspondence with degassing spots and fumaroles. The layers filling the excavated depression and covering the surrounding undisturbed ground consist of variably altered and reworked materials from the second group (E1–E3). The contact layers of the third group (C1 and C2) generally separate these two types of layers. Often, sulphur-cemented grounds develop on top of the reworked material filling the depression. The temperature in layers below such cemented grounds ranges between 26°C and 38°C within the first 15–20 cm and increases to 66°C–87°C at a depth >50 cm (s1—s7). Above the ground and in the proximity of degassing spots (e1 and e2), temperatures can vary between 31°C and 80°C. Southwest of domain 1, layers of Taupo Pumice covered by modern soil layers of the fourth group (O) are predominant (e3—e5 in Figure 8 and Table 1). Generally, their alteration state increases in the proximity of degassing features (e.g., fumaroles), as shown by exposed profile e5a–e5c, where dominant T2 gradually

passes into T3–T5. Here, the temperature of the measured layers within the first 30 cm increases to 55°C and 93°C (e5a–e5c).

In domain 2, soils within the depressed areas are dominated by sinter formation and mud deposits (e.g., M layers; s8, e7, and e8 in Figure 8 and Table 1). The surrounding rims are instead characterised by unaltered to moderately altered Taupo Pumice layers. For instance, layers T1–T3, covered by modern soil layer (O), can be found on the rim of the site 8 depression, at locations e8s and e8n. Soil layer temperatures are generally low and range between 15°C and 24°C within 45–130 cm from the ground level.

In domain 3, subsoils show a similar sequence to that observed in the excavated sites along domain 1, but with altered layers being more abundant. For instance, at exposed profiles e9–e14, the highly altered T4 is often found below T3, which is in turn covered by C1 and C2 or by modern O layers (Figure 9; Table 1). Layer temperature ranges between 12°C and 44°C within 180 cm, while it can increase to 89–97°C in the first 30–40 cm below the ground. Close to fumaroles (e.g., at e14), the temperature above the ground reaches 56°C and 74°C within the first 60 cm, whereas in the presence of sulphur-rich layers (e.g., at e9), the temperature can decrease from >90 to <50°C (Figure 9; Table 1).

In areas with the cold sulphur-cemented ground, north of the DOC thermal area (e.g., s9 and s10 at site 13), subsoils below the sulphur-cemented crusts comprise excavated material (E1–E3) overlaying Taupo Pumice (T) and/or breccia deposit (Br) layers. The temperature of the layers quickly increases to 64–94°C below the crusts but is normally <40°C within the low-permeable, firm breccia material (Figure 9; Table 1).

Partial measurements possible around collapsed structures of domains 1 and 3 (Figures 4A–D; Figure 6) showed that the top and subsoils were mostly moderately to highly altered Taupo Pumice such as T3 and T5.

4.3.3 Soil-embedded pumices

Pumices are widely distributed throughout the field, and especially those with granule to boulder size represent a dominant component of many recognised soil layers. In addition to being found as reworked pumices (or pumiceous material) in subsoil layers and hard grounds, they are more often located *in situ* within the Taupo Pumice deposit. We measured permeability, porosity, and density of unaltered and altered (sulphur-bearing) pumices along an exposed transect (e3, e4, and e5) southwest of domain 1 (Figure 8 and Supplementary Tables S1, S2). Unaltered to weakly altered pumices are very permeable, with values ranging between 1.2×10^{-13} and 1×10^{-11} m^2, whereas their moderately to highly altered counterpart shows permeability between 5.3×10^{-15} and 6.5×10^{-13} m^2. In terms of porosity, unaltered pumice shows a very similar range (57.5%–64.1%) compared to the sulphur-bearing clasts (60.6%–61%), whereas the density of the former is slightly higher (0.9–1.2 g/cm^3) than that of the latter (0.8–0.9 g/cm^3). It is to be noted that the measured porosity and density of sulphur-cemented pumice from pumiceous mounds (s1 and s5 samples in Supplementary Table S2) are less porous (22.4%–47%) and can be denser (up to 1.4 g/cm^3).

4.4 Main hard ground types

4.4.1 Sulphur-cemented grounds

Three main types of sulphur-cemented ground were recognised in the field based on their texture, structures, and physical properties (Figure 11 and Supplementary Figures S7, S8 and Supplementary Tables S1, S2). Generally, the sulphur-cemented grounds develop on top of either *in situ* Taupo Pumice deposits or over mixed reworked materials (clay–sand or granule–pebble dominated) related to the mining activities. The first type is flat cemented grounds consisting of hard layers >5–25 cm thick, tabular in shape, distributed over large areas or found in small patches, with surficial patinas and degassing cracks. Surficial patinas can be very fine-grained or show a coarser grain texture (Figure 11A and Supplementary Figures S7A, B). The second type is crusted hummocks, which are mound-shaped structures characterised by a surficial fine- to coarse-grained patina, the presence of cracks, and several small degassing vents. Native sulphur occurs typically as yellow encrustations at these fumarolic vents and along cracks (Figure 11B and Supplementary Figures S7C–E). The third type includes cemented pumiceous mounds and tread tracks. These are abundant around excavated areas with the heated and degassing ground where the precipitation of sulphur encrusts both reworked materials and tracks left by mining machinery (Figure 11D and Supplementary Figures S7F–H). In areas of intense degassing, pumiceous mounds can grow by sulphur precipitation and form patina and cracks similar to hummocky grounds. Wrinkle-like features and fractures are very common and lie parallel to the main cracks, showing a spreading of soils occurring around the central cracks. Overall, it appears that sulphur precipitation is more abundant in coarse-grained levels, independent of the ground type.

The permeability of flat cemented grounds measured in spots without the surficial patina varies between 4×10^{-15} and 8×10^{-12} m^2, with lower values associated with the presence of compact silty or sulphur-rich levels (Figure 11A and Supplementary Table S1). In both heated ground and cold areas, degassing pathways or sulphur-bearing fractures linked to surficial cracks are observed in the soil layers below the encrusted grounds (Figures 11A, B). Crusted hummocks have permeability ranging between 1.5×10^{-16} and 1.3×10^{-12} m^2, depending on the presence of silty vs. coarse-grained levels within their structure. Degassing pathways cross the soil layers below crusted hummocks and are connected to surficial cracks or vents (Figures 11C–E). In the pumiceous mounds, the permeability is highly variable depending on the dominant component and ranges from 8×10^{-15} to 8×10^{-13} m^2 for variably cemented clay–sand portions (Figure 11F); from 1.7×10^{-15} to 7.4×10^{-13} m^2 for sulphur-bearing pumiceous pebbles and cobbles; and from 2.2 to 3.5×10^{-12} m2 for sulphur-free pumices (see site 2 values in Supplementary Table S1). In all the sulphur-cemented types of ground, the presence of surficial patinas can strongly reduce permeability, as shown by measured values ranging between 2.5×10^{-15} and 5×10^{-13} m^2 (Supplementary Table S1).

The porosity and density of selected sulphur-cemented samples from flat, hummocky, and pumiceous mounds show a wide range of values, reflecting the inner structure of the samples, the degree of cementation, and the dominant grain sizes. The measured samples are representative of warmer and highly degassing sites close to site 1 and of colder crusts in mildly heated grounds surrounding site 13. In warmer areas, the crusted material has a variable porosity (13.5%–30.9%) and density (2.1–2.4 g/cm^3), with the more porous sample showing a texture of porous course-grained clasts cemented by coarse sulphur grains. In colder areas, cemented crusts show a porosity of 17.2%–19.3% and a density of 2.1 g/cm^3, mirroring a fine-grained texture of the cement and more widespread sulphur precipitation (Supplementary Figure S8 and Supplementary Table S2).

TABLE 1 Soil properties for all measured profiles (see location in Figures 8, 9 and Supplementary Figure S1). Sample names are included where permeability measurements correspond to a specific layer. Soil layers are described in the text. For a few of the measured soil profiles, some of the parameters were not measured due to the samples being unconsolidated or showing too high temperature and humidity for the instrument. For exposed sections, height values are positive above the ground level.

Soil (s)/exposure (e)	Soil type	k [m^2]	T [°C]	σ [kg/cm^2]	τ [kg/cm^2]	Porosity [%]	Height [cm]
s1	E1	2.4×10^{-14}	66	2.6	2.8	47	-70
	E2	4×10^{-15}	22	3.0	4.8	11	-55
	E2	1.4×10^{-14}	38	3.1	4.6	58	-35
	E2	6×10^{-15}	36	3.1	4.6	-	-35
	E3	4.5×10^{-15}	26	5.2	2.6	64	-20
s2	E1	$<5.6\times10^{-16}$	53	4.2	2.2	-	-60
	E2	1.4×10^{-14}	43	4.4	3.0	29	-35
	E3	-	-	3.9	3.1	-	-10
s3	E1	2.1×10^{-15}	49	5.5	3.4	32	-35
	E2	8.1×10^{-15}	38	5.5	3.2	54	-20
s4	T3	2.1×10^{-14}	57	4.3	4.0	69	-30
	T3	5.7×10^{-13}	38	1.4	1.9	37	10
	C1	1.7×10^{-14}	41	0.2	2.5	41	10
	C2	9×10^{-14}	34	0.9	3.3	44	50
	C2	2.7×10^{-14}	34	0.9	3.3	44	50
s5	E3	2.7×10^{-13}	88	3.0	2.5	11	-45
	E3	2.8×10^{-14}	20	5.5	7.5	65	-40
	E2	3.7×10^{-14}	55	3.9	2.6	20	-20
	E3	7.2×10^{-14}	61	1.0	1.9	4	-15
	E2	1.9×10^{-14}	58	5.4	4.3	39	-10
s8	M	2.8×10^{-15}	14	4.0	2.8	56	-48
	M	$<5.6\times10^{-16}$	11	5.2	6.9	50	-35
	M	7.5×10^{-16}	10	4.2	7.1	95	-25
s9	T3	2.9×10^{-13}	94	1.8	0.7	-	-65
	E2	1.1×10^{-14}	75	3.7	3.7	19	-55
	-	-	-	-	-	-	-40
	E3	8.5×10^{-15}	48	5.5	5.7	11	-20
s10	Br	9.4×10^{-16}	40	3.0	2.9	21	-55
	E1	2.9×10^{-13}	64	5.3	4.2	18	-45
	E2	5.8×10^{-15}	47	4.4	3.6	6	-15
e1	T3	-	74	3.4	4.8	-	5
	T4	-	46	1.2	2.9	-	45
	C2	-	40	0.9	0.9	-	80
	C2	-	31	0.6	0.9	-	125
e2	T5	8.7×10^{-13}	87	0.2	0.6	46	-15
	T3	1.1×10^{-14}	80	1.1	0.9	34	30
	C1	4.3×10^{-15}	63	-	-	34	50
	C2	4.4×10^{-13}	55	0.0	0.7	17	75

(Continued on following page)

TABLE 1 (*Continued*) Soil properties for all measured profiles (see location in Figures 8, 9 and Supplementary Figure S1). Sample names are included where permeability measurements correspond to a specific layer. Soil layers are described in the text. For a few of the measured soil profiles, some of the parameters were not measured due to the samples being unconsolidated or showing too high temperature and humidity for the instrument. For exposed sections, height values are positive above the ground level.

Soil (s)/exposure (e)	Soil type	k [m^2]	T [°C]	σ [kg/cm^2]	τ [kg/cm^2]	Porosity [%]	Height [cm]
e3	T1	1.7×10^{-14}	14	5.5	4.0	16	10
	T1	4.3×10^{-15}	13	5.5	4.7	19	165
	T1	7×10^{-14}	13	3.7	3.3	11	300
e4	T2	7.1×10^{-14}	20	4.2	5.0	18	45
	T2	6.6×10^{-15}	15	3.5	6.4	20	105
	T2	3.2×10^{-15}	13	5.5	7.4	35	145
e5a	T3	1.9×10^{-14}	59	3.5	4.7	22	5
e5b	T2	1.1×10^{-15}	65	5.5	4.7	33	-25
	O	4.1×10^{-14}	55	4.2	6.7	22	5
e5c	T5	3.2×10^{-15}	84	5.0	5.8	49	-30
	T3	1.4×10^{-13}	93	3.1	4.7	57	-20
e6	M	$<5.6\times10^{-16}$	55	3.0	4.8	65	-35
	M	$<5.6\times10^{-16}$	19	1.0	2.8	79	-20
e7	O	3.8×10^{-14}	12	2.5	1.7	16	-10
	O	1.1×10^{-13}	12	1.8	1.5	19	10
	O	1.5×10^{-13}	10	1.7	1.7	18	25
	O	1.9×10^{-13}	8	1.5	2.5	25	35
e8n	T2	5.3×10^{-15}	22	4.5	1.5	-	45
	T2	-	18	5.5	3.6	—	85
	O	2.1×10^{-14}	15	3.0	2.4	-	125
e8s	T3	1.1×10^{-15}	24	5.5	3.1	-	50
	O	5.7×10^{-15}	19	1.7	2.3	-	130
e9	T4	-	97	1.3	1.3	-	5
	T3	-	50	1.2	2.9	-	70
e10	T4	-	44	2.2	2.1	-	20
	T4	-	33	2.3	2.3	-	60
	T3	-	31	2.9	3.7	-	80
	C1	-	22	0.7	2.5	-	95
	C2	-	26	0.2	1.0	-	110
e11	T4	-	21	3.4	1.4	-	20
	T3	-	16	3.0	3.4	-	60
	O	—	14	3.3	3.1	-	90
e12	T3	-	63	5.3	3.1	-	-10
	T3	-	35	0.3	1.5	-	30
	C2	-	29	1.5	1.7	-	50
	C1	-	23	0.7	1.9	-	75
	C1	-	21	0.8	1.9	-	90

(Continued on following page)

TABLE 1 (*Continued*) Soil properties for all measured profiles (see location in Figures 8, 9 and Supplementary Figure S1). Sample names are included where permeability measurements correspond to a specific layer. Soil layers are described in the text. For a few of the measured soil profiles, some of the parameters were not measured due to the samples being unconsolidated or showing too high temperature and humidity for the instrument. For exposed sections, height values are positive above the ground level.

Soil (s)/exposure (e)	Soil type	*k* [m^2]	T [°C]	σ [kg/cm^2]	τ [kg/cm^2]	Porosity [%]	Height [cm]
e13	T3	-	52	5.5	3.3	-	0
	T3	-	24	2.0	2.3	-	60
	T3	-	22	0.2	1.0	-	100
	C2	-	12	0.4	1.0	-	140
e14	T3	-	89	4.5	2.3	-	-10
	T3	-	74	0.7	1.5	-	20
	C1	-	68	0.6	2.5	-	27
	C2	-	56	0.1	1.7	-	60

k, permeability; T, soil temperature; σ, compressive strength; and τ, shear strength.

4.4.2 Stromatolites and silica sinters

At the Lagoon, stromatolites and silica sinters are the dominant ground type. In the eastern part of the Lagoon, at site 5, stromatolitic deposits form bands 1–2 m wide that lie parallel to the shoreline (Figures 12A–C). They form two to three zones, including 1) spicular to small diameter (<5 mm) columnar stromatolites with increasing height away from the pools; 2) upward expanding blade-shaped stromatolites, with blades perpendicular to the shoreline and forming a distinct ridge that is higher than the columnar stromatolites; and 3) scattered columnar stromatolites (up to 1 cm high), clusters of bulbous stromatolites, or smooth, flat sinter surfaces (Figures 12A, B). The inner structure of stromatolites is laminated (Figure 12C). The surficial permeability of stromatolites, where measurable on smooth surfaces, ranges between 4.2×10^{-15} and 1.4×10^{-14} m^2 (Supplementary Figure S9A and Supplementary Table S2).

In the western and central portions (sites 6 and 7), silica sinters are made of alternating layers of green, yellow, and grey muds with different degrees of cementation (Figure 5D, 12d–g and Supplementary Figures S9B–D). Such deposits were found to be composed of kaolinite, elemental sulphur, alunite, and amorphous silica and commonly contain many diatoms according to Krupp and Seward (1987). A deposit of relict sinters >1-m-thick outcrops on a side of the excavated area at site 9 is buried beneath reworked materials. Such outcrops and scattered blocks around the site indicate a wider distribution of the sinter deposits than at present, before mining activity. The upper portions of sinters are richer in granular material more typical of outflow deposits (Figure 12H), likely indicating a lowering of spring level in time at this site. The field-measured surficial permeability ranges between 8.4×10^{-15} and 1.5×10^{-14} m^2. Porosities and permeability of some of the most representative samples measured in the laboratory, instead, are in the range of 65%–78% and 1×10^{-14} to 7×10^{-12} m^2, respectively (Supplementary Figures S9A–D).

4.5 Surface temperatures

Surface temperatures in the Rotokawa DOC thermal area range from 20 to >90°C. The map of temperature distribution in subsoils and springs/pools shown in Figure 13 was obtained by using the nearest neighbour interpolation and manually adjusted to better fit the modelled isolines when they deviated strongly from the data points. Elevated surface temperatures from 80 to >90°C were only measured at vents of active fumaroles or at collapsed structures, such as those along domains 1 and 3. Some other isolated spots showing high temperatures are found north of the DOC thermal area (e.g., at site 13).

Temperatures >50°C are common for many of the springs and pools along domains 1 and 2. Interestingly, temperature profiles in exposed sections of the Lagoon's site 7 show an increase from <30 to >50°C below sinters and/or hardened clay layers. We used the values measured from many of the spring and pool waters (>95°C) to estimate the temperature distribution at the Lagoon.

In areas with steaming and heated ground, temperatures >50°C could be measured from cracks in the cemented grounds, while surrounding patinas are colder than 30°C. Many of the areas covered by sulphur-cemented ground, distributed in the central part of the DOC thermal area and in the northern portion of the lagoon, are generally colder than 20–30°C.

5 Discussion

5.1 Distribution of thermal features

At the surface, geothermal manifestations are limited to specific zones, and the alteration effects derived from diffuse degassing typical of many of these thermal features decrease rapidly in magnitude with distance. Thermal features may have been more limited in extension in pre-mining times, but likely distributed in the same areas where we observe thermal manifestation (Bardsley and Williams, 2017). Following the sulphur mining activities, new thermal features rapidly superimposed where the land surface was excavated and/or a confining low-permeable cap removed.

Diffuse degassing *via* fumaroles occurs all over the three domains within the DOC thermal area and outside. Fumarolic manifestations vary from isolated sulphur-encrusted vents to cracks in cemented grounds. In areas of intense degassing of sulphur-rich gases, native

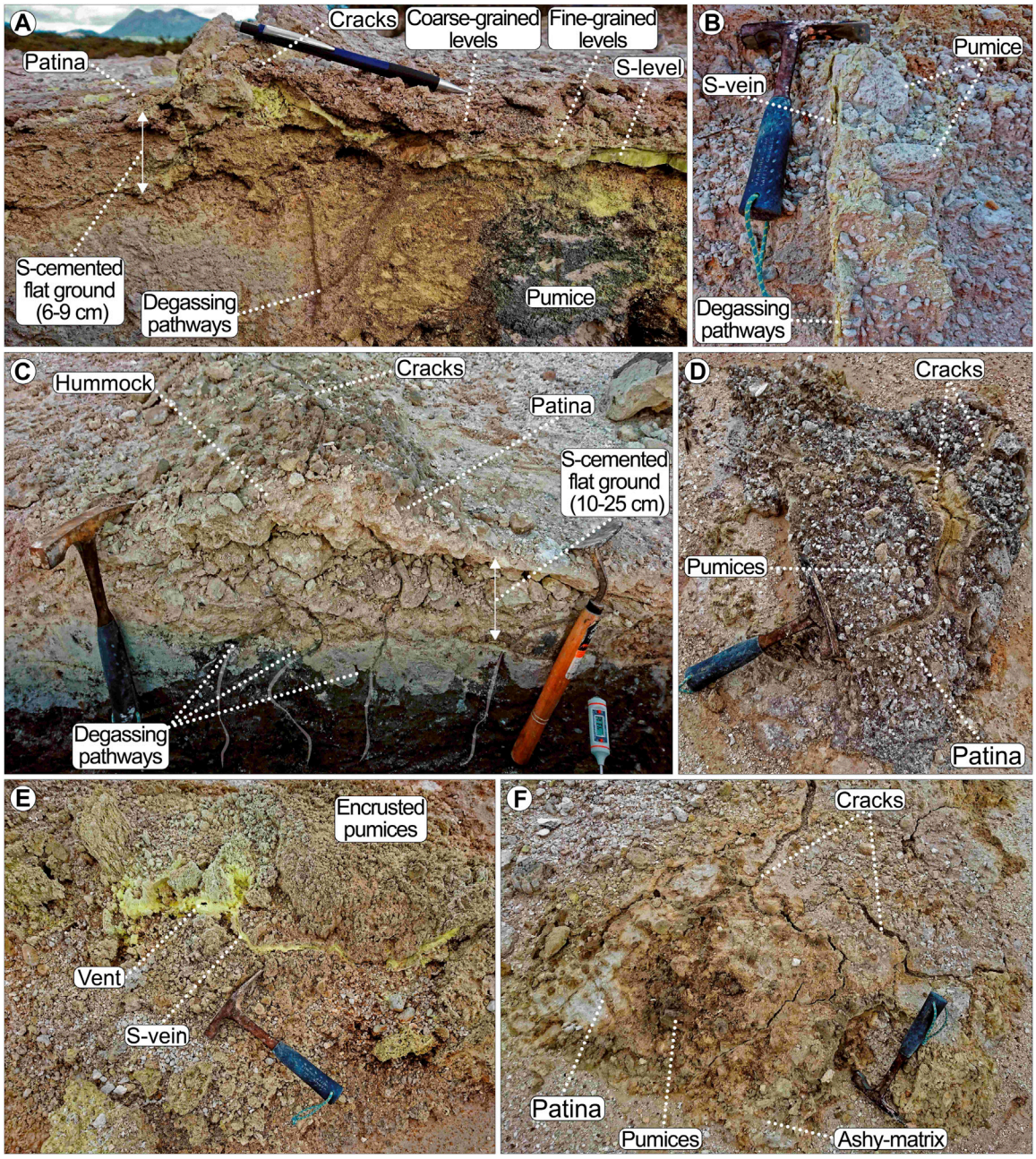

FIGURE 11
Structures and components of sulphur-cemented grounds. **(A)** Flat cemented ground section showing the presence in the crust structure of fine-grained silty or sulphur layers. A series of degassing pathways or sulphur-bearing fractures are observed in the soil layers below the encrusted grounds, as rooted in surficial cracks. **(B)** Example of a sulphur-bearing fracture. **(C–F)** Section and examples of crusted hummocks and pumiceous mounds. The section shows the alternation of silty and coarse-grained layers with the central growing portion and a surficial patina covering the hummock. Similar to flat grounds, degassing pathways are crossing the soil layers below the crusted hummocks and appear connected to surficial cracks or vents.

sulphur is deposited in permeable sandy or pebble-rich layers, forming crusted grounds with or without abundant pumices. In the case of highly degassing spots or areas, the sulphur crystal growth pushed apart the ground materials to form bulging mounds (hummocks) made of exfoliating yellow sulphurous crusts (Cody, 2003; Piochi et al., 2015; Montanaro et al., 2017). Mined areas show abundant encrusted structures (including tread tracks) and hummocks of different shapes, sizes, and components, all indicating rapid precipitation of sulphur minerals after excavations/disturbances (Labrado et al., 2019; Pirajno, 2020). In case of intense degassing along a geological discontinuity (e.g., between the Taupo Pumice deposit and older bedrock at site 12), the acidic leaching resulted in the formation of collapsed structures, unstable ground, and multiple fumarole vents (Isaia et al., 2015; Kanakiya et al., 2021; Troiano et al., 2021).

Individual or coalesced warm-to-hot springs and pools are found mostly close to Lake Rotokawa, as well as in deeply excavated sites (e.g., sites 3–9) and collapsed structures intersecting the water table (e.g., sites 19–22). The upflow of sulphate–chloride waters in these

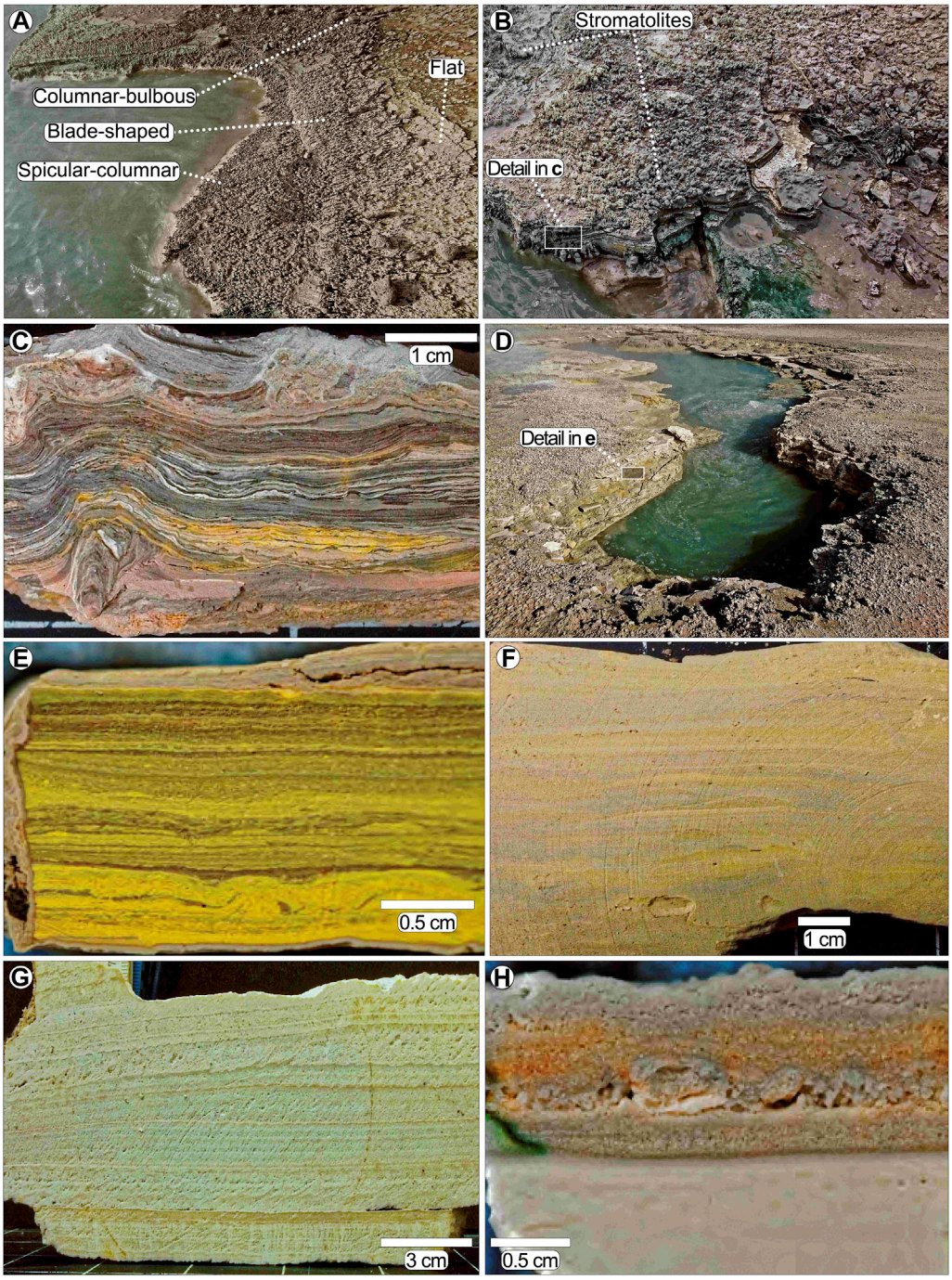

FIGURE 12
Sections and components of sinters from site 5 **(A–C)**, sites 6 and 7 **(D–G)**, and site 9 **(H)**. **(A–C)** Microbial mats and siliceous stromatolites with characteristic morphologies (spicular–columnar, blade-shaped, and columnar bulbous) and fine laminated texture are formed east of the hot pools at site 5. **(E–G)** Sites 6 and 7 are dominated by muddy and laminated sinter deposits with different degrees of cementation and abundance in granular material. **(H)** Relict silica sinters made of an alternation of very fine silt and sandy, porous level are found buried at site 9 by the reworked material.

areas causes mineral precipitation of silica sinters, clays, and zeolites, while variation in groundwater levels and proliferation of bacteria change the sulphur oxidation rates to favour sulphur precipitation (Krupp and Seward, 1987; Jones et al., 2000; Rodgers et al., 2002). In hotter spots (e.g., site 5), precipitation begins around pool margins with the build-up of siliceous stromatolites, composed of opaline silica, kaolinite, and native sulphur (Krupp and Seward, 1987; Jones et al., 2000). The laminated muds around the Lagoon (e.g., sites 6 and 7) are instead formed by the deposition of muddy sediments, diatoms, and minerals during the outflow period of warm water (Renaut and Jones, 2011; Montanaro et al., 2017). Active spots of acid springs producing silica sinters can also be found along the Pararikі Stream at the Mars Flat (Schinteie et al., 2007). Areas of past sinter deposition (or paleosurfaces; Sillitoe 2015) include site 9, where sinter formed

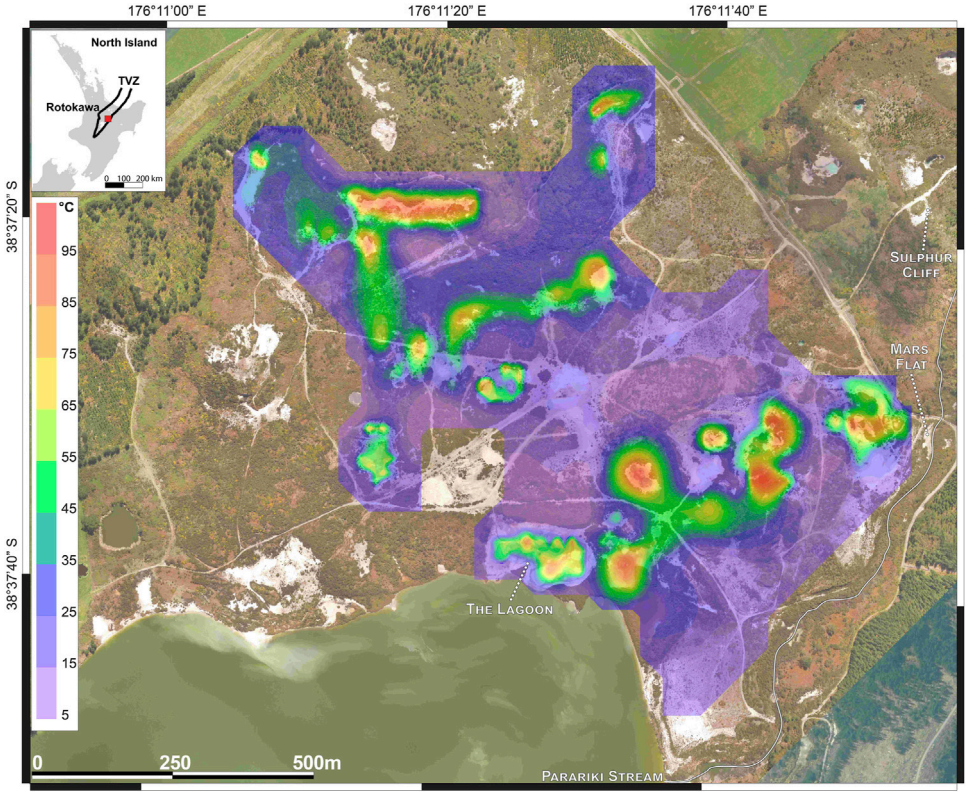

FIGURE 13
Map of surface temperatures including both near-surface soil (<15 cm) and water temperatures (see also Supplementary Figure S1A). Soils and cemented/hard ground temperatures were measured using a digital thermocouple (0.01°C accuracy). Water temperatures of springs and pools were measured using a wired thermocouple (0.01°C accuracy) fully submerged in water as close as possible to the bubbling vent area.

slightly above (≥1 m) the actual groundwater level; sites 19–22, where sinter likely formed in a steam-heated environment before the growth of collapsed structures.

Many of the depressions in the western part of the DOC thermal area (e.g., at site 9) and southwest of domain 1 (e.g., sites 3 and 4) contain abundant mud pots that are dominated by fine-grained sediments suspended in the water columns accumulating on their floors. These mud-rich waters are the products of rock dissolution by hot, acidic fluids (Delmelle and Bernard, 1994; Hedenquist and Taran, 2013; Hedenquist et al., 2017; Hedenquist et al., 2021), and their finely laminated sediments are known to contain amorphous silica along with sulphates such as gypsum, barite, anatase, native sulphur, and pyrite (Rodgers et al., 2002; Rodgers et al., 2004).

Most of the DOC thermal area terrain and the thermal ground northeast of it rise to >10 and >20 m above the groundwater table, respectively (Supplementary Figure S1B). In these vadose zones, the reactive H_2S-bearing steam condensate causes advanced argillic steam-heated alteration, producing native sulphur, together with clay-rich and hydrothermally altered rocks that are weak and prone to mechanical failure (Frolova et al., 2014; Mayer et al., 2017; Mordensky et al., 2018; Frolova et al., 2019). In the thicker vadose portions, the intense leaching of material from the subsurface—just above the groundwater table—likely generated subsurface cavities, whose destabilisation led to formation of the large collapse structures observed in domains 1 (e.g., at site 1) and 3 (e.g., at site 10) and at sites 19–22 (Sillitoe, 2015; Al-Halbouni et al., 2018).

In all the domains, the presence of hard ground types thicker than 10–15 cm appears to buffer the heat flow at the subsoil level (Figure 3; Figure 13). These sulphur-cemented ground and associated surficial patinas act as efficient thermal insulators that can locally mask elevated subsoil temperatures (up to 80–90°C).

5.2 Distribution of soils

Soils in undisturbed and altered areas developed within the Taupo Pumice, and their characteristics are controlled by the structure of the original flow deposit, which is made of alternating slightly consolidated, fine-grained (ash-dominated), and coarse-grained (pumice-dominated), poorly consolidated layers (Figure 14). Generally, a dark, low-porous and mid-to-low permeability vegetated topsoil layer made of silt/sand (layer O) is found above subsoil layers that range from being silty to pebble/boulder-rich (Figures 7, 10). In the mined areas—both in the excavated sections and on spoil piles at the sides—soil layers developed in reworked material with variable grain sizes and degrees of alteration (from an unaltered to a highly altered state) produced by rising fluids in pre-excavation times (e.g., at site 2). In natural-occurring, highly degassing collapsed features formed where lithological and/or structural discontinuity are present (e.g., at site 12), soils are essentially made of weakly to highly altered Taupo Pumice, mostly reduced to friable, unstable, locally cemented, clayey material.

In both undisturbed and excavated/reworked settings, silt- and sand-rich layers have low-to-medium porosity and permeability, variable compaction, and degree of alteration (Figures 10, 14; Table 1). Slightly compacted ash-rich layers (T1) in undisturbed sites have low porosity and mid-to-low permeability and typify stable, cold ground. In areas with thermal manifestations and mild degassing activity, the properties of ash-rich soils are degrading toward fumarole vents: more porous and mid-to-highly permeable, slightly compacted ash-rich layers (T2) are found away from degassing vents. Loosely compacted, friable layers (T3) with mid-to-high porosity and mid-to-low permeability are characterising vent areas. Layers rich in unaltered pebble- /boulder-sized pumices have mid-to-high porosity and high permeability, whereas sites with mild to intense degassing activity and layers rich in altered and degraded pumices (T4–T5) show lower porosity and permeability. Backfill and reworked piles around excavated areas are often made of silt-to-pebble-sized ashy/pumiceous material differently altered (E1–E3) that show mid-to-high porosity and low-to-high permeability. In some of the hottest and intensively altered excavated sites (e.g., site 2), highly altered, low-to-mid porous, and low-to-high permeable clayey material (C1 and C2) is found between *in situ* and reworked materials. These layers probably derive from the excavation and piling of highly altered soils near fumarolic areas. Depressions with springs and mud pools (e.g., at site 8) are paved and dominated by laminated soils with very low-permeable dark clays (M). In the north, mining activity exposed warm-cemented breccia (Br) that is dominated by heterolithic products of hydrothermal eruptions.

5.3 Relationship between thermal features and soil types

Conceptual cross sections cutting through sites within domains 1, 2, and 3, showing the main relationship between the different thermal features and soil patterns within the DOC thermal area, are given in Figure 14. The relationship between the different domains and their soils and hard ground properties (permeability, temperature, and strength of the individual layers) reflects the interaction of the hydrothermal system with the subsurface geology and mining activities. A clear distinction in features appears between areas located approximately at the water table level (334.5–335 m) and areas 10 and 20 m above it in the steam-heated portions (Figure 14A). In the former areas, the deposition of mud deposits, sinters, and stromatolites around warm springs and mud pools dominates within excavated sites. In the vadose portions, the leaching and degradation of the Taupo Pumice produce broad, unstable grounds and collapse structures in proximity or above fractures, while extensive formation of sulphur-encrusted grounds and sulphur-rich soils occurs in excavated sites (Figures 14B, C).

Overall, the natural and mining-derived geothermal features correspond to the areas of low-to-intense degassing recognised by Bloomberg et al. (2014). Their distribution along linear and circular patterns suggests a strong connection with subsurface faults or eruption crater rims (Curewitz and Karson, 1997; Schöpa et al., 2011; Germa et al., 2013; Báez et al., 2017; D'Elia et al., 2020; Montanaro et al., 2021). The high concentration of collapsed structures and the widespread unstable grounds aligned along an NE–SW direction likely reflect the intense processes of leaching and dissolution produced by fluids rising from the main field fault system (e.g., the Central and Injection Faults in Figure 1; Wallis et al., 2013). Other thermal features aligned in the E–W direction (e.g., at site 12) or distributed along circular patterns (e.g., features around sites 8, 10, 11, and 19–22) can result from fluids rising through fractured portions adjacent to the eruption crater (Roberts et al., 2011; Bloomberg et al., 2014; Isaia et al., 2015). The presence of fractures propagating through the Taupo Pumice deposit (Whelley et al., 2012) and lithological discontinuity between the pumice flow and bedrock/breccia deposits around the DOC thermal area (Collar, 1985) represent other pathways that facilitated the vertical diffusion of fluids (Figures 14A, B).

Properties of investigated top and subsoil layers show that degraded and clay-rich soils produced by alteration in a geothermal environment represent very weak and low-permeability units that can affect the degassing of hydrothermal active areas (del Potro and Hürlimann, 2009; Harris et al., 2012; Montanaro et al., 2017). Altered soils rich in clay observed in the close vicinity of degassing vents or depositing within depressions dominated by mud pools (Figure 4; Figure 5; Figure 10) could further contribute to a decrease in permeability and create a "sealing" effect close to the surface (Mayer et al., 2017; Frolova et al., 2019). On the other hand, an abundance of unaltered to weakly altered, permeable pumice-rich layers within the Taupo Pumice likely allowed arising fluids to rapidly migrate both vertically and horizontally (Heap et al., 2017; Jácome-Paz et al., 2020). Moreover, the diffusion of acid gases within poorly consolidated, permeable pumice-rich soils and/or backfill and reworked piles further favoured leaching processes that resulted in the formation of highly unstable, sinking grounds (Churchman and Lowe, 2012; Cigna et al., 2019), one of the most spatially distributed features within the DOC thermal area (Figure 3).

In concert with other studies from the Valley of Desolation in Dominica Island (Mayer et al., 2017), Solfatara in Campi Flegrei (Montanaro et al., 2017), several fields in the Kamchatka Peninsula (Frolova et al., 2019; Frolova et al., 2020a), and Whakaari (White Island) in New Zealand (Heap et al., 2017), our results show the important role of top and subsoil in modulating surficial degassing processes within geothermal environments.

5.4 Geothermal hazard implication

Hydrothermal alteration observed at the Rotokawa DOC thermal area resulted from two main processes, i.e., leaching or precipitation, with opposite influences on porosity, permeability, and strength (Pola et al., 2012; Frolova et al., 2014; Mayer et al., 2016; Mordensky et al., 2019). Such changes in petrophysical and mechanical properties of rocks in shallow portions of geothermal areas can have important implications for ground deformation hazards (e.g., unstable grounds, sinkholes, and subsidence; Bromley et al., 2015; Frolova et al., 2020a).

A quite evident effect is the intense leaching of Taupo Pumice and the formation of collapsing structures. Some of the unstable ground areas can likely represent sites of future collapse. Risks may also derive from hidden cavities below the sulphur-encrusted ground. Cavity enlargement due to intensified acidic alteration during strong rain periods can lead to sinkhole formations, yielding lethal threats when gas-filled, as in the tragic accident at Campi Flegrei's Solfatara (Italy) in September 2017 (Costa et al., 2022). Another important implication due to subsoil alteration is related to the development of subsidence anomalies. The past occurrence of such phenomena at Rotokawa has

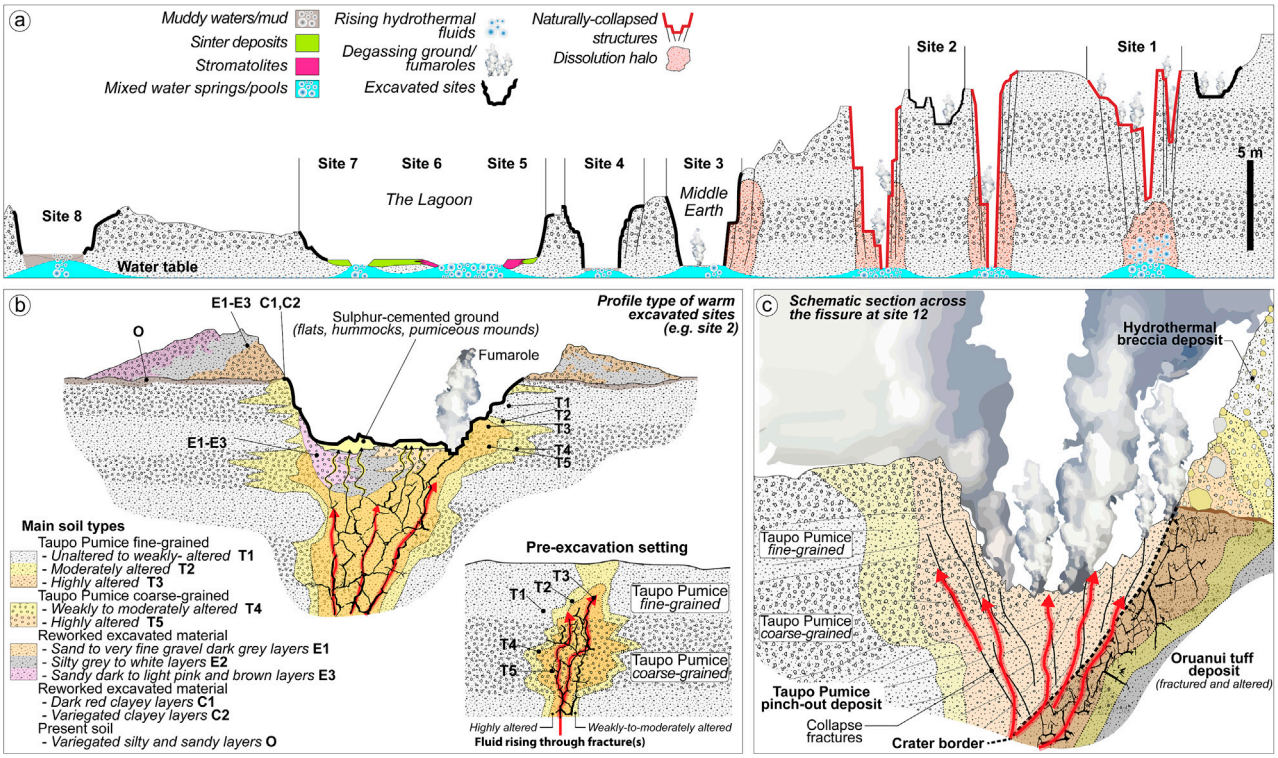

FIGURE 14
Conceptual sections of typical geothermal features and domains in the DOC thermal area. **(A)** Typical profile for excavated areas such as at site 2. Idealised pre-excavation profile is also shown. **(B)** Profile of subsoil and deeper structure in areas of degassing through a significant geological/structural contact (e.g., at site 12). **(C)** Profile of the variation of geothermal features from water and muddy waters/mud in the proximity of Lake Rotokawa (e.g., sites 5–8) up to the collapsed and degassing structures forming in the relatively higher terrain (up to 11 and 16 m above the water table.

been suggested by Powell (2011) based on the modelling of levelling data from the 1950s (i.e., before geothermal development). However, the causes of the subsidence were attributed to the alteration of deeper reservoir rocks, resulting in porosity development, and the natural subsidence was inferred to be due to the gradual collapse of this pore space. Subsidence with a relatively shallow (<50 m) origin has instead been reported from the nearby Tauhara geothermal field (Bromley et al., 2009). In this case, the combined presence of intensely altered, highly compressible ignimbrite below the hydrothermal breccia deposit and the lowering of water levels in a shallow boiling aquifer caused ground deformation. In particular, the failure of porous silicified pyroclastic material initiated the subsidence, which has been later intensified by the compaction of highly degraded and clay-altered pumice-rich levels of the ignimbrite. If the intense steam-heated alteration observed at the Rotokawa DOC thermal area became extensive at depth, for instance, along geological contacts, faults, or in gas-rich permeable layers (Heap et al., 2017; Frolova et al., 2020a), it may result in the formation of intensely degraded, clay-rich layers and porous sulphur-cemented layers, which can be prone to compaction, potentially causing subsidence.

6 Conclusion

The geothermal activity across the DOC thermal area within the Rotokawa geothermal field reflects the complex interaction between the underlying hydrothermal system, regional faults, shallow explosive crater, and subsurface geology, which has been further modified by recent mining activities. Combined field and laboratory methods allowed us to evaluate the type and pattern of superposed hydrothermal features and alteration of soils developed after mining activities and assess their role in the degassing processes. The spatial distribution of all thermal features and soils generally relates to the local and regional geological and structural settings and the occurrence of mining, perturbating the circulation of surficial fluids.

Together with isolated thermal spots scattered around the DOC thermal area, three domains with characteristic thermal features are located in the eastern, central, and northern parts of the DOC thermal area:

1) Domain 1 has numerous features aligned along an NW–SE direction. In its central and NE portions, there are abundant natural collapse structures with and without springs and pools at their base and excavated areas with sulphur-cemented grounds and fumarolic activity. In the W and SW portions, warm springs and pools of mixed compositions and mud pots characterise depressed areas produced by mining activity.
2) Domain 2 includes the Lagoon with two sub-areas of depositional environments (eastern hot pools forming sinters, microbial mats and stromatolites, and western/central springs depositing muddy and laminated sinters) and two other depressions dominated by bubbling mud pools, unstable grounds, and warm springs with old sinter deposits.

3) Domain 3 shows widespread degassing features, sulphur-cemented, and unstable grounds. In this domain lies the hottest feature in the whole DOC thermal area, consisting of a W–E-oriented fissure with highly altered, friable and unstable ground with collapsing rims. Such a thermal feature developed along geological discontinuities (explosive crater rim) where the ignimbrite deposits (Taupo Pumice) overlie the local bedrock (altered Oruanui ignimbrite and Pararikі Breccia).

We also provide the first detailed top and subsoil stratigraphy and a map of the Rotokawa DOC thermal area, supported by a robust dataset of petrophysical and mechanical soil properties. Soil layers develop mostly in the Taupo Pumice and reworked material and were grouped into five different main categories according to the environment in which they occur (undisturbed vs. reworked and unaltered vs. altered), as well as depending on their granulometry and average petrophysical and mechanical properties. Generally, but not in a linear manner for all layers, the increase in alteration intensity is accompanied by an increase in porosity and permeability and a decrease in strength. Other soil types consist of low permeable and hard sulphur-cemented grounds and silica sinters that are found as a top layer in many excavated sites or surrounding springs and isolated heterolithic breccia.

Surface temperatures (<15 cm) range from approximately ~20 to >90°C. Elevated values (80 to >90°C) are only measured at vents of active fumaroles, or at collapsed structures, while >50°C are common for many of the springs and pools. In many areas, the presence of colder (<30°C) topsoil layers, such as sulphur-cemented ground, sinters, and/or hardened clay, appears to buffer the heat flow from a hotter (>50°C) subsoil.

We found that within excavated areas close to the water table, the acidic fluids produced deposits of mud, sinters, and stromatolites around warm springs and mud pools. In the vadose, steam-heated portions, fluids degrade the Taupo Pumice, promoting formation of unstable grounds and collapse structures, as well as extensive deposition of sulphur within the soils of excavated sites. In this setting, the dominant layer and alteration type can strongly control the fluid circulation and surfacing within the top and subsoils. Moreover, our results highlight the importance of sulphur precipitation within steam-heated zones of geothermal environments, especially if perturbed by mining. We observe that pumiceous and more permeable soil layers within the *in situ* Taupo Pumice and reworked material can act as lateral/vertical fluid pathways. On the contrary, the presence of lower permeability layers (e.g., clay/silt rich) in the subsoil, and/or the formation of silica sinters and sulphur-cemented, hard grounds, can inhibit surficial fluid degassing.

Rotokawa's DOC thermal area is one peculiar geothermal spot where changes of permeability in the very shallow portions (top–subsoils) of the hydrothermal system were produced by both natural (alteration) and anthropic (mining) processes and resulted in rapid changes and/or migration of thermal features. Such changes can further evolve in the future, bearing potential hazards that include the formation of new unstable grounds, localised ground collapses, and larger-scale subsidence. The results presented in this study may be considered a contribution to new methods for monitoring changes in surficial thermal features and soil properties, which can improve the assessment of geothermal hazards in similar environments.

Data availability statement

The original contributions presented in the study are included in the article/Supplementary Material; further inquiries can be directed to the corresponding author.

Author contributions

CM led the project and wrote the manuscript draft with help from LR. Fieldwork mapping, measurements, and sample collection were carried out by CM, LR, BS, SR, and SC. LR performed the laboratory measurements of porosity and density with help from BS and CM. CM and LR worked on the realisation of the maps. All authors contributed to the writing of the manuscript.

Funding

CM was supported by the Deutsche Forschungsgemeinschaft under grant MO3508/1-1. CM, SC, and BS acknowledge funding from the New Zealand Ministry of Business, Innovation, and Employment, Smart Ideas grant for "Stable power generation and tourism with reduced geothermal explosion hazard" UOAX1807.

Acknowledgments

The authors gratefully acknowledge the Rotokawa Joint Venture partnership between Tauhara North No. 2 Trust and Mercury NZ Ltd. for their support and permission to publish this paper. We also acknowledge the Ngati Tahu-Ngati Whaoa Runanga Trust as mana whenua of the Rotokawa DOC thermal area and thank the Trust (particularly Johlene Kelly) and the New Zealand Department of Conservation (Te Papa Atawhai and particularly Harry Keys) who supported this research.

Conflict of interest

AC and CB were employed by Mercury NZ Ltd.

The remaining authors declare that the research was conducted in the absence of any commercial or financial relationships that could be construed as a potential conflict of interest.

Publisher's note

Supplementary material

The Supplementary Material for this article can be found online at: https://www.frontiersin.org/articles/10.3389/feart.2022.1067012/full#supplementary-material

References

Addison, S. J., Winick, J. A., Mountain, B. W., and Siega, F. L. (2015). "Rotokawa reservoir tracer test history," in Proceedings, 37th New Zealand Geothermal Workshop, Taupo, New Zealand, 18–20 Nov 2015, 1–10.

Al-Halbouni, D., P Holohan, E., Taheri, A., Schöpfer, M. P. J., Emam, S., and Dahm, T. (2018). Geomechanical modelling of sinkhole development using distinct elements: Model verification for a single void space and application to the Dead Sea area. *Solid earth.* 9, 1341–1373. doi:10.5194/se-9-1341-2018

Allis, R., Bromley, C., and Currie, S. (2009). Update on subsidence at the Wairakei-Tauhara geothermal system, New Zealand. *Geothermics* 38, 169–180. doi:10.1016/j.geothermics.2008.12.006

Ármannsson, H., Fridriksson, T., Wiese, F., Hernández, P., and Pérez, N. (2007). "CO2 budget of the Krafla geothermal system, NE-Iceland," in *Proceedings of the 12th international symposium on water-rock interaction* (London: Taylor & Francis Group), 189–192.

Aubert, M., Diliberto, S., Finizola, A., Ch, Y., Aubert, M., Diliberto, S., et al. (2009). Double origin of hydrothermal convective flux variations in the Fossa of Vulcano (Italy). *Bull. Volcanol.* 70, 1–14. doi:10.1007/s00445-007-0165-y

Báez, W., Carrasco Nuñez, G., Giordano, G., Viramonte, J. G., and Chiodi, A. (2017). Polycyclic scoria cones of the Antofagasta de la Sierra basin, Southern Puna plateau, Argentina. *Geol. Soc. Spec. Publ.* 446, 311–336. doi:10.1144/SP446.3

Bagnato, E., Barra, M., Cardellini, C., Chiodini, G., Parello, F., and Sprovieri, M. (2014). First combined flux chamber survey of mercury and CO2 emissions from soil diffuse degassing at Solfatara of Pozzuoli crater, Campi Flegrei (Italy): Mapping and quantification of gas release. *J. Volcanol. Geotherm. Res.* 289, 26–40. doi:10.1016/j.jvolgeores.2014.10.017

Bardsley, C., and Williams, K. (2017). The dawn of Rotokawa: Lines on the land (map series 2). Available at: https://mrpmaps.maps.arcgis.com/apps/MapSeries/index.html?appid=2595f98e263d4f4db895bbe0694e2938 (Accessed January 5, 2023).

Basmanov, O. L., Kiryukhin, A. V., Maguskin, M. A., Dvigalo, V. N., and Rutqvist, J. (2016). Thermo-hydrogeomechanical modeling of vertical ground deformation during the operation of the Mutnovskii Geothermal Field. *J. Volcanol. Seismol.* 10, 138–149. doi:10.1134/S0742046316020032

Bloomberg, S., Werner, C., Rissmann, C., Mazot, A., Horton, T., Gravley, D., et al. (2014). Soil CO2 emissions as a proxy for heat andmass flow assessment, Taupo Volcanic Zone, New Zealand. *Am. Geophys. Union Geochem. Geophys. Geosystems* 15, 4885–4904. doi:10.1002/2014GC005327

Bromley, C. J., Currie, S., Jolly, S., and Mannington, W. (2015). "Subsidence: An update on New Zealand geothermal deformation observations and mechanisms," in Proc World Geothermal Congress 2015, Melbourne, Australia 1, 19–25.

Bromley, C. J., Currie, S., Manville, V. R., and Rosenberg, M. D. (2009). Recent ground subsidence at Crown Road, Tauhara and its probable causes. *Geothermics* 38, 181–191. doi:10.1016/j.geothermics.2008.11.008

Brooks-Clarke, I. (2021). *Mineralogical insights into hydrothermal eruption conditions at the Rotokawa Geothermal Field*. MSC. thesis (New Zealand: School of Environment, University of Auckland).

Brown, S. E., Pregitzer, K. S., Reed, D. D., and Burton, A. J. (2000). Predicting daily mean soil temperature from daily mean air temperature in four northern hardwood forest stands. *For. Sci.* 46, 297–301. doi:10.1093/forestscience/46.2.297

Browne, P. R. L. (1988). Exploration of the Rotokawa geothermal field, Taupo volcanic zone, New Zealand. *Conf. Geotherm. Res. Soc. Jpn.*, 1–6.

Browne, P. R. L. (1989). Investigations at the Rotokawa geothermal field, Taupo volcanic zone, New Zealand. *J. Geotherm. Res. Soc. Jpn.* 11, 87–96.

Browne, P. R. L., and Lawless, J. V. (2001). Characteristics of hydrothermal eruptions, with examples from New Zealand and elsewhere. *Earth Sci. Rev.* 52, 299–331. doi:10.1016/S0012-8252(00)00030-1

Calibugan, A., Melia, K., and Rivera, M. (2022). "Conceptual model update for the Rotokawa geothermal field, New Zealand," in Proceedings 44th New Zealand Geothermal Workshop. Auckland, New Zealand, 8.

Carapezza, M. L., Barberi, F., Ranaldi, M., Ricci, T., Tarchini, L., Barrancos, J., et al. (2011). Diffuse CO2 soil degassing and CO2 and H2S concentrations in air and related hazards at Vulcano Island (Aeolian arc, Italy). *J. Volcanol. Geotherm. Res.* 207, 130–144. doi:10.1016/j.jvolgeores.2011.06.010

Chambefort, I. (2021). Sulfur in New Zealand geothermal systems: insights from stable isotope and trace element analyses of anhydrite from Rotokawa and Ngatamariki geothermal fields, Taupo Volcanic Zone. *New Zeal. J. Geol. Geophys.* 64, 372–388. doi:10.1080/00288306.2020.1851265

Chiodini, G., Caliro, S., Cardellini, C., Granieri, D., Avino, R., Baldini, a., et al. (2010). Long-term variations of the Campi Flegrei, Italy, volcanic system as revealed by the monitoring of hydrothermal activity. *J. Geophys. Res. Solid Earth* 115, 1–17. doi:10.1029/2008JB006258

Chiodini, G., Cioni, R., Marini, L., and Panichi, C. (1995). Origin of the fumarolic fluids of Vulcano Island, Italy and implications for volcanic surveillance. *Bull. Volcanol.* 57, 99–110. doi:10.1007/bf00301400

Churchman, G. J., and Lowe, D. J. (2012). "Alteration, formation, and occurrence of minerals in soils introduction: The role of mineralogy in soil science," in *Handbook of soil sciences*. 2nd Ed. (Boca Raton, FL: CRC Press, Taylor & Francis), 1, 20.1–20.72.

Cigna, F., Tapete, D., Garduño-Monroy, V. H., Muñiz-Jauregui, J. A., García-Hernández, O. H., and Jiménez-Haro, A. (2019). Wide-area InSAR survey of surface deformation in urban areas and geothermal fields in the eastern Trans-Mexican Volcanic Belt, Mexico. *Remote Sens.* 11, 1–33. doi:10.3390/rs11202341

Cody, A. D. (2003). Geology, history and stratigraphy of hydrothermal eruptions in the rotorua geothermal field. Available at: https://hdl.handle.net/10289/7696 (Accessed January 5, 2023).

Collar, R. J., and Browne, P. R. L. (1985). "Hydrothermal eruptions at tie Rotokawa geothermal field, Taupo volcanic zone, New Zealand," in *Proceedings. 7th NZ geothermal workshop*. Auckland, New Zealand: University of Auckland, 171–175.

Collar, R. J. (1985). *Hydrothermal eruptions in the Rotokawa geothermal system*. New Zealand: Unpubl. Geothermal Institute Report, University of Auckland.

Costa, A., Di Vito, M. A., Ricciardi, G. P., Smith, V. C., and Talamo, P. (2022). The long and intertwined record of humans and the Campi Flegrei volcano (Italy). *Bull. Volcanol.* 84, 5–27. doi:10.1007/s00445-021-01503-x

Curewitz, D., and Karson, J. A. (1997). Structural settings of hydrothermal outflow: Fracture permeability maintained by fault propagation and interaction. *J. Volcanol. Geotherm. Res.* 79, 149–168. doi:10.1016/S0377-0273(97)00027-9

Daskalopoulou, K., Gagliano, A. L., Calabrese, S., Li Vigni, L., Longo, M., Kyriakopoulos, K., et al. (2019). Degassing at the volcanic/geothermal system of kos (Greece): Geochemical characterization of the released gases and CO2 output estimation. *Geofluids* 2019, 3041037. doi:10.1155/2019/3041037

del Potro, R., and Hürlimann, M. (2009). The decrease in the shear strength of volcanic materials with argillic hydrothermal alteration, insights from the summit region of Teide stratovolcano, Tenerife. *Eng. Geol.* 104, 135–143. doi:10.1016/j.enggeo.2008.09.005

D'Elia, L., Páez, G., Hernando, I. R., Petrinovic, I. A., López, L., Kürten, G., et al. (2020). Hydrothermal eruptions at El Humazo, Domuyo geothermal field, Argentina: Insights into the eruptive dynamics and controls. *J. Volcanol. Geotherm. Res.* 393, 106786. doi:10.1016/j.jvolgeores.2020.106786

Delmelle, P., and Bernard, A. (1994). Geochemistry, mineralogy, and chemical modeling of the acid crater lake of Kawah Ijen Volcano, Indonesia. *Geochim. Cosmochim. Acta* 58, 2445–2460. doi:10.1016/0016-7037(94)90023-X

Dempsey, D. E., Rowland, J. V., Zyvoloski, G. A., and Archer, R. A. (2012). Modeling the effects of silica deposition and fault rupture on natural geothermal systems. *J. Geophys. Res. Solid Earth* 117, 1–18. doi:10.1029/2012JB009218

Farquhar, G., Crawford, S., High, R., and Anderson, S. (2001). *New Zealand geotechnical society guideline for hand held shear vane test*. NZ Geotechnical Society Inc. Available at: https://www.nzgs.org/libraries/guideline-for-hand-held-shear-vane-test/ (Accessed January 5, 2023).

Frolova, J., Chernov, M., Rychagov, S., Kuznetsov, R., and Surovtseva, K. (2019). Alteration of volcanic rocks and changes in physical-mechanical properties on the South-Kambalny thermal field (South Kamchatka). *E3S Web Conf.* 98, 08002. doi:10.1051/e3sconf/20199808002

Frolova, J., Ladygin, V., Rychagov, S., and Zukhubaya, D. (2014). Effects of hydrothermal alterations on physical and mechanical properties of rocks in the Kuril-Kamchatka island arc. *Eng. Geol.* 183, 80–95. doi:10.1016/j.enggeo.2014.10.011

Frolova, J. V., Chernov, M. S., Kuznetsov, R. A., Ladygin, V. M., and Sokolov, V. N. (2020a). The influence of hydrothermal argillization on the physical and mechanical properties of tuffaceous rocks: A case study from the upper pauzhetsky thermal field, Kamchatka. *Bull. Eng. Geol. Environ.* 80, 1635–1651. doi:10.1007/s10064-020-02007-2

Frolova, J. V., Chernov, M. S., Rychagov, S. N., and Zerkal, O. V. (2020b). "The impact of hydrothermal activity on the geological environment, Kamchatka Peninsula," in *World geothermal congress*, 1–14.

Frolova, Y. V., Rychagov, S. N., Ladygin, V. M., Luchko, M. V., Chernov, M. S., and Boikova, I. A. (2016). Variation in the physical and mechanical properties of rocks: The North Paramushir hydrothermal magmatic system, Kuril Islands. *J. Volcanol. Seismol.* 10, 170–187. doi:10.1134/S0742046316030039

Germa, A., Connor, L. J., Cañon-Tapia, E., and Le Corvec, N. (2013). Tectonic and magmatic controls on the location of post-subduction monogenetic volcanoes in Baja California, Mexico, revealed through spatial analysis of eruptive vents. *Bull. Volcanol.* 75, 782–814. doi:10.1007/s00445-013-0782-6

Giggenbach, W. F. (1995). Variations in the chemical and isotopic composition of fluids discharged from the Taupo Volcanic Zone, New Zealand. *J. Volcanol. Geotherm. Res.* 68, 89–116. doi:10.1016/0377-0273(95)00009-J

Gresse, M., Vandemeulebrouck, J., Byrdina, S., Chiodini, G., and Bruno, P. P. (2016). Changes in CO2 diffuse degassing induced by the passing of seismic waves. *J. Volcanol. Geotherm. Res.* 320, 12–18. doi:10.1016/j.jvolgeores.2016.04.019

Gvozdeva, I. P., Frolova, J. V., and Zerkal, O. V. (2015). "Slope processes hazards in geothermal areas: A case study of the geysers valley, Kamchatka," in *World geothermal congress*, 19–25.

Harris, A., Alparone, S., Bonforte, A., Dehn, J., Gambino, S., Lodato, L., et al. (2012). Vent temperature trends at the Vulcano Fossa fumarole field: The role of permeability. *Bull. Volcanol.* 74, 1293–1311. doi:10.1007/s00445-012-0593-1

Harris, A. J. L., and Maciejewski, A. J. H. (2000). Thermal surveys of the vulcano fossa fumarole field 1994 - 1999: Evidence for fumarole migration and sealing. *J. Volcanol. Geotherm. Res.* 102, 119–147. doi:10.1016/s0377-0273(00)00184-0

Healy, J. (1975). "Volcanic lakes," in *New Zealand lakes*. Editors V. H. Jolly and J. M. Brown (New Zealand: Auckland University Press), 70–83.

Heap, M. J., Baumann, T. S., Rosas-Carbajal, M., Komorowski, J., Gilg, H. A., Villeneuve, M., et al. (2021). Alteration-induced volcano instability at La Soufrière de Guadeloupe (Eastern Caribbean). *J. Geophys. Res. Solid Earth* 126. doi:10.1029/2021jb022514

Heap, M. J., Kennedy, B. M., Farquharson, J. I., Ashworth, J., Mayer, K., Letham-Brake, M., et al. (2017). A multidisciplinary approach to quantify the permeability of the Whakaari/White Island volcanic hydrothermal system (Taupo Volcanic Zone, New Zealand). *J. Volcanol. Geotherm. Res.* 332, 88–108. doi:10.1016/j.jvolgeores.2016.12.004

Heap, M. J., Kennedy, B. M., Pernin, N., Jacquemard, L., Baud, P., Farquharson, J. I., et al. (2015). Mechanical behaviour and failure modes in the Whakaari (White Island volcano) hydrothermal system, New Zealand. *J. Volcanol. Geotherm. Res.* 295, 26–42. doi:10.1016/j.jvolgeores.2015.02.012

Hedenquist, J., Arribas, A., and Hedenquist, J. (2021). Exploration implications of multiple formation environments of advanced argillic minerals. *Econ. Geol.* 117, 609–643. doi:10.5382/econgeo.4880

Hedenquist, J. W., Arribas, R., A., and Aoki, M. (2017). Zonation of sulfate and sulfide minerals and isotopic composition in the far southeast porphyry and lepanto epithermal Cu–Au deposits, Philippines. *Resour. Geol.* 67, 174–196. doi:10.1111/rge.12127

Hedenquist, J. W., and Taran, Y. A. (2013). Modeling the formation of advanced argillic lithocaps: Volcanic vapor condensation above porphyry intrusions. *Econ. Geol.* 108, 1523–1540. doi:10.2113/econgeo.108.7.1523

Hopp, C., Sewell, S., Mroczek, S., Savage, M., and Townend, J. (2020). Seismic response to evolving injection at the Rotokawa geothermal field, New Zealand. *Geothermics* 85, 101750. doi:10.1016/j.geothermics.2019.101750

Inguaggiato, S., Diliberto, I. S., Federico, C., Paonita, A., and Vita, F. (2018). Review of the evolution of geochemical monitoring, networks and methodologies applied to the volcanoes of the Aeolian Arc (Italy). *Earth-Science Rev.* 176, 241–276. doi:10.1016/j.earscirev.2017.09.006

Isaia, R., Vitale, S., Di Giuseppe, M. G., Iannuzzi, E., D'Assisi Tramparulo, F., and Troiano, a. (2015). Stratigraphy, structure, and volcano-tectonic evolution of Solfatara maar-diatreme (Campi Flegrei, Italy). *Geol. Soc. Am. Bull.* 127, 1485–1504. doi:10.1130/B31183.1

Jácome-Paz, M. P., González-Romo, I. A., Prol-Ledesma, R. M., Torres Vera, M. A., Pérez-Zárate, D., Rodríguez-Díaz, A. A., et al. (2020). Multivariate analysis of CO2, H2S and CH4 diffuse degassing and correlation with fault systems in Agua Caliente - tzitzio, Michoacán, México. *J. Volcanol. Geotherm. Res.* 394, 106808. doi:10.1016/j.jvolgeores.2020.106808

Jentsch, A., Jolie, E., Jones, D. G., Taylor-Curran, H., Peiffer, L., Zimmer, M., et al. (2020). Magmatic volatiles to assess permeable volcano-tectonic structures in the Los Humeros geothermal field, Mexico. *J. Volcanol. Geotherm. Res.* 394, 106820. doi:10.1016/j.jvolgeores.2020.106820

John, D. A., Sisson, T. W., Breit, G. N., Rye, R. O., and Vallance, J. W. (2008). Characteristics, extent and origin of hydrothermal alteration at Mount Rainier Volcano, Cascades Arc, USA: Implications for debris-flow hazards and mineral deposits. *J. Volcanol. Geotherm. Res.* 175, 289–314. doi:10.1016/j.jvolgeores.2008.04.004

Jones, B., Renaut, R. W., and Rosen, M. R. (2000). Stromatolites forming in acidic hot-spring waters, North Island, New Zealand. *Palaios* 15, 450–475. doi:10.1669/0883-1351(2000)015<0450:SFIAHS>2.0.CO;2

Jury, A. P. (1984). "The Rotokawa sulphur deposits," in *Proceedings 18th annual australasian institute of mining and metallurgy New Zealand branch conference*, 192–205.

Kanakiya, S., Adam, L., Rowe, M. C., Lindsay, J. M., and Esteban, L. (2021). The role of tuffs in sealing volcanic conduits. *Geophys. Res. Lett.* 48. doi:10.1029/2021gl095175

Kiryukhin, A. V., Vorozheikina, L. A., Voronin, P., and Kiryukhin, P. A. (2017). Thermal and permeability structure and recharge conditions of the low temperature Paratunsky geothermal reservoirs in Kamchatka, Russia. *Geothermics* 70, 47–61. doi:10.1016/j.geothermics.2017.06.002

Koros, W., O'Sullivan, J., Pogacnik, J., O'Sullivan, M., Pender, M., and Bromley, C. (2015). "Variability of geotechnical properties of materials within wairakei subsidence bowl, New Zealand," in Proceedings 37th New Zealand geothermal workshop, November 18-20, 2015. Taupo, New Zealand. Auckland, New Zealand: University of Auckland, 1–8.

Kristianto, B., Gunderson, R., and Gunawan, A. (2013). "Geological engineering for hazard assessment of pad awi-14, salak field, west java, Indonesia," in *Indonesian geothermal association conference 2013*, 1–7.

Krupp, R. E., and Seward, T. M. (1987). The Rotokawa geothermal system, New Zealand: An active epithermal gold-depositing environment. *Econ. Geol.* 4, 1109–1129. doi:10.2113/gsecongeo.82.5.1109

Labrado, A. L., Brunner, B., Bernasconi, S. M., and Peckmann, J. (2019). Formation of large native sulfur deposits does not require molecular oxygen. *Front. Microbiol.* 10, 24–26. doi:10.3389/fmicb.2019.00024

Leonard, G. S. S., Begg, J. G. G., and Wilson, C. J. J. J. N. (2010). *Geology of the rotorua area*. Lower Hutt: Institute of Geological & Nuclear Sciences Limited: Institute of Geological & Nuclear Sciences.

Lynne, B. Y., Pender, M., Glynn-Morris, T., and Sepulveda, F. (2013). Combining scanning electron microscopy and compressibility measurement to understand subsurface processes leading to subsidence at Tauhara Geothermal Field, New Zealand. *Eng. Geol.* 166, 26–38. doi:10.1016/j.enggeo.2013.08.008

Madonia, P., Cangemi, M., Costa, M., and Madonia, I. (2016). Mapping fumarolic fields in volcanic areas: A methodological approach based on the case study of La fossa cone, vulcano island (Italy). *J. Volcanol. Geotherm. Res.* 324, 1–7. doi:10.1016/j.jvolgeores.2016.05.014

Marini, L., Principe, C., Chiodini, G., Cioni, R., Fytikas, M., and Marinelli, G. (1993). Hydrothermal eruptions of Nisyros (Dodecanese, Greece). Past events and present hazard. *J. Volcanol. Geotherm. Res.* 56, 71–94. doi:10.1016/0377-0273(93)90051-r

Mayer, K., Scheu, B., Gilg, H. A., Heap, M. J., Kennedy, B. M., Lavallée, Y., et al. (2015). Experimental constraints on phreatic eruption processes at Whakaari (White Island volcano). *J. Volcanol. Geotherm. Res.* 302, 150–162. doi:10.1016/j.jvolgeores.2015.06.014

Mayer, K., Scheu, B., Montanaro, C., Yilmaz, T. I. T. I., Isaia, R., Aßbichler, D., et al. (2016). Hydrothermal alteration of surficial rocks at Solfatara (Campi Flegrei): Petrophysical properties and implications for phreatic eruption processes. *J. Volcanol. Geotherm. Res.* 320, 128–143. doi:10.1016/j.jvolgeores.2016.04.020

Mayer, K., Scheu, B., Yilmaz, T. I., Montanaro, C., Albert Gilg, H., Rott, S., et al. (2017). Phreatic activity and hydrothermal alteration in the Valley of desolation, Dominica, lesser antilles. *Bull. Volcanol.* 79, 82. doi:10.1007/s00445-017-1166-0

McNamara, D. D., Sewell, S., Buscarlet, E., and Wallis, I. C. (2016). A review of the Rotokawa geothermal field, New Zealand. *Geothermics* 59, 281–293. doi:10.1016/j.geothermics.2015.07.007

Milicich, S. D., Chambefort, I., Simpson, M. P., Wilson, C. J. N., Alcaraz, S., Bardsley, C., et al. (2020a). "Geology, geochronology, alteration and geochemistry of the Rotokawa Geothermal System, Taupō Volcanic Zone, New Zealand," in *Proceedings world geothermal congress*, 1–12.

Milicich, S. D., Chambefort, I., Wilson, C. J. N., Alcaraz, S., Ireland, T. R., Bardsley, C., et al. (2020b). A zircon U-Pb geochronology for the Rotokawa geothermal system, New Zealand, with implications for Taupō Volcanic Zone evolution. *J. Volcanol. Geotherm. Res.* 389, 106729. doi:10.1016/j.jvolgeores.2019.106729

Milicich, S. D., and Hunt, T. (2007). Thermal features of the Rotokawa geothermal field. *GNS Sci. Consult. Rep.* 90, 2007.

Montanaro, C., Mayer, K., Isaia, R., Gresse, M., Scheu, B., Ylmaz, T. I., et al. (2017). Hydrothermal activity and subsoil complexity: Implication for degassing processes at Solfatara crater, Campi Flegrei caldera. *Bull. Volcanol.* 79, 83. doi:10.1007/s00445-017-1167-z

Montanaro, C., Mortensen, K. A., Weisenberger, T. B., Dingwell, D. B., and Scheu, B. (2021). Stratigraphic reconstruction of the víti breccia at krafla volcano (Iceland): Insights into pre-eruptive conditions priming explosive eruptions in geothermal areas. *Bull. Volcanol.* 83, 81–27. doi:10.1007/s00445-021-01502-y

Mordensky, S. P., Heap, M. J., Kennedy, B. M., Gilg, H. A., Villeneuve, M. C., Farquharson, J. I., et al. (2019). Influence of alteration on the mechanical behaviour and failure mode of andesite: Implications for shallow seismicity and volcano monitoring. *Bull. Volcanol.* 44, 44. doi:10.1007/s00445-019-1306-9

Mordensky, S. P., Villeneuve, M. C., Kennedy, B. M., Heap, M. J., Gravley, D. M., Farquharson, J. I., et al. (2018). Physical and mechanical property relationships of a shallow intrusion and volcanic host rock, Pinnacle Ridge, Mt. Ruapehu, New Zealand. *J. Volcanol. Geotherm. Res.* 359, 1–20. doi:10.1016/j.jvolgeores.2018.05.020

Mormone, A., Tramelli, A., Di Vito, M. a., Piochi, M., Troise, C., and Natale, G. D. (2011). Secondary hydrothermal minerals in buried rocks at the Campi Flegrei caldera, Italy: A possible tool to understand the rock-physics and to assess the state of the volcanic system. *Period. Miner.* 80, 385–406. doi:10.2451/2011PM0027

Mormone, A., Troise, C., Piochi, M., Balassone, G., Joachimski, M., De Natale, G., et al. (2015). Mineralogical, geochemical and isotopic features of tuffs from the CFDDP drill hole: Hydrothermal activity in the eastern side of the Campi Flegrei volcano (southern Italy). *J. Volcanol. Geotherm. Res.* 290, 39–52. doi:10.1016/j.jvolgeores.2014.12.003

Pantaleo, M., and Walter, T. R. (2014). The ring-shaped thermal field of stefanos crater, nisyros island: A conceptual model. *Solid earth.* 5, 183–198. doi:10.5194/se-5-183-2014

Pedone, M., Viveiros, F., Aiuppa, A., Giudice, G., Grassa, F., Gagliano, A. L., et al. (2015). Total (fumarolic + diffuse soil) CO2 output from Furnas volcano. *Earth, Planets Sp.* 67, 174. doi:10.1186/s40623-015-0345-5

Peiffer, L., Carrasco-Núñez, G., Mazot, A., Villanueva-Estrada, R. E., Inguaggiato, C., Bernard Romero, R., et al. (2018). Soil degassing at the Los Humeros geothermal field (Mexico). *J. Volcanol. Geotherm. Res.* 356, 163–174. doi:10.1016/j.jvolgeores.2018.03.001

Peruzzetto, M., Komorowski, J. C., Le Friant, A., Rosas-Carbajal, M., Mangeney, A., and Legendre, Y. (2019). Modeling of partial dome collapse of La soufrière of Guadeloupe volcano: Implications for hazard assessment and monitoring. *Sci. Rep.* 9, 13105–13116. doi:10.1038/s41598-019-49507-0

Piochi, M., Mormone, A., Balassone, G., Strauss, H., Troise, C., and De Natale, G. (2015). Native sulfur, sulfates and sulfides from the active Campi Flegrei volcano (southern Italy): Genetic environments and degassing dynamics revealed by mineralogy and isotope geochemistry. *J. Volcanol. Geotherm. Res.* 304, 180–193. doi:10.1016/j.jvolgeores.2015.08.017

Pirajno, F. (2020). Subaerial hot springs and near-surface hydrothermal mineral systems past and present, and possible extraterrestrial analogues. *Geosci. Front.* 11, 1549–1569. doi:10.1016/j.gsf.2020.04.001

Pola, A., Crosta, G. B., Fusi, N., and Castellanza, R. (2014). General characterization of the mechanical behaviour of different volcanic rocks with respect to alteration. *Eng. Geol.* 169, 1–13. doi:10.1016/j.enggeo.2013.11.011

Pola, A., Crosta, G., Fusi, N., Barberini, V., and Norini, G. (2012). Influence of alteration on physical properties of volcanic rocks. *Tectonophysics* 566–567, 67–86. doi:10.1016/j.tecto.2012.07.017

Powell, T. (2011). Natural subsidence at the Rotokawa geothermal field and implications for permeability development. *Trans. - Geotherm. Resour. Counc.* 35 (2), 973–976.

Price, L., Powell, T. S., and Atkinson, L. (2011). Geothermal fluid evolution at Rotokawa: Hydrothermal alteration indicators. *Trans. - Geotherm. Resour. Counc.* 35 (2), 977–982.

Procter, J. N., Cronin, S. J., Zernack, a. V., Lube, G., Stewart, R. B., Nemeth, K., et al. (2014). Debris flow evolution and the activation of an explosive hydrothermal system; Te Maari, Tongariro, New Zealand. *J. Volcanol. Geotherm. Res.* 286, 303–316. doi:10.1016/j.jvolgeores.2014.07.006

Reid, M. E., Sisson, T. W., and Brien, D. L. (2002). Volcano collapse promoted by hydrothermal alteration and edifice shape, Mount Rainier, Washington. *Geology* 29, 779–782. doi:10.1130/0091-7613(2001)029<0779:VCPBHA>2.0.CO;2

Renaut, R. W., and Jones, B. (2011). "Hydrothermal environments, terrestrial," in *Encyclopedia of geobiology*. Editors J. Reitner and V. Thiel, (Dordrecht: Springer), 467–479. doi:10.1007/978-1-4020-9212-1_114

Revil, A., Coperey, A., Heap, M. J., and Carbillet, L. (2020). A geophysical index to map alteration, permeability, and mechanical properties within volcanoes. Application to the soft volcanic rocks from Whakaari/White Island (New Zealand). *J. Volcanol. Geotherm. Res.* 401, 106945. doi:10.1016/j.jvolgeores.2020.106945

Ricci, T., Finizola, A., Barde-Cabusson, S., Delcher, E., Alparone, S., Gambino, S., et al. (2015). Hydrothermal fluid flow disruptions evidenced by subsurface changes in heat transfer modality: The La Fossa cone of Vulcano (Italy) case study. *Geology* 43, 959–962. doi:10.1130/G37015.1

Risk, G. F. (2000). "Electrical resistivity surveys of the Rotokawa geothermal field, New Zealand," in *Proceedings of the 22th New Zealand geothermal workshop*. Auckland, New Zealand: University of Auckland, 121–126.

Robb, L. (2004). in *Introduction to ore-forming processes*. Editor L. Robb (Oxford: Blackwell Publishing).

Roberts, K. S., Davies, R. J., Stewart, S. A., and Tingay, M. (2011). Structural controls on mud volcano vent distributions: Examples from Azerbaijan and Lusi, east Java. *J. Geol. Soc. Lond.* 168, 1013–1030. doi:10.1144/0016-76492010-158

Rodgers, K. A., Browne, P. R. L., Buddle, T. F., Cook, K. L., Greatrex, R. A., Newton, Z., et al. (2004). Silica phases in sinters and residues from geothermal fields of New Zealand. *Earth-Science Rev.* 66, 1–61. doi:10.1016/j.earscirev.2003.10.001

Rodgers, K. A., Cook, K. L., Browne, P. R. L., and Campbell, K. A. (2002). The mineralogy, texture and significance of silica derived from alteration by steam condensate in three New Zealand geothermal fields. *Clay Min.* 37, 299–322. doi:10.1180/0009855023720035

Rott, S., Scheu, B., Montanaro, C., Mayer, K., Joseph, E. P., and Dingwell, D. B. (2019). Hydrothermal eruptions at unstable crater lakes: Insights from the boiling lake, Dominica, lesser antilles. *J. Volcanol. Geotherm. Res.* 381, 101–118. doi:10.1016/j.jvolgeores.2019.05.020

Rowland, J., Bardsley, C., Downs, D., Sepúlveda, F., Simmons, S., and Scholz, C. (2012). "Tectonic controls on hydrothermal fluid flow in a rifting and migrating arc, Taupo Volcanic Zone, New Zealand," in *Proceedings of the 34th New Zealand geothermal workshop*. Auckland, New Zealand: University of Auckland, 6.

Rowland, J. V., and Simmons, S. F. (2012). Hydrologic, magmatic, and tectonic controls on hydrothermal flow, Taupo Volcanic Zone, New Zealand: Implications for the formation of epithermal vein deposits. *Econ. Geol.* 107, 427–457. doi:10.2113/econgeo.107.3.427

Samsonov, S., Beavan, J., González, P. J., Tiampo, K., and Fernández, J. (2011). Ground deformation in the Taupo volcanic zone, New Zealand, observed by ALOS PALSAR interferometry. *Geophys. J. Int.* 187, 147–160. doi:10.1111/j.1365-246X.2011.05129.x

Schinteie, R., Campbell, K. A., and Browne, P. R. L. (2007). Microfacies of stromatolitic sinter from acid-sulphate-chloride springs at Parariki Stream, Rotokawa geothermal field, New Zealand. *Palaeontol. Electron.* 10, 1–33.

Schöpa, A., Pantaleo, M., and Walter, T. R. (2011). Scale-dependent location of hydrothermal vents: Stress field models and infrared field observations on the Fossa Cone, Vulcano Island, Italy. *J. Volcanol. Geotherm. Res.* 203, 133–145. doi:10.1016/j.jvolgeores.2011.03.008

Scott, B. (2012). *Guideline for mapping and monitoring geothermal features*. Whakatāne, New Zealand: Bay of Plenty Regional Council, 35.

Shen, L. C., Wu, K. Y., Xiao, Q., and Yuan, D. X. (2011). Carbon dioxide degassing flux from two geothermal fields in Tibet, China. *Chin. Sci. Bull.* 56, 3783–3793. doi:10.1007/s11434-011-4352-z

Sillitoe, R. H. (2015). Epithermal paleosurfaces. *Min. Depos.* 50, 767–793. doi:10.1007/s00126-015-0614-z

Simpson, M. P., Morales, A. G., Chambefort, I., Alcaraz, S., Moribe, S., Milicich, S. D., et al. (2021). "Hydrothermal minerals and hydrologic evolution of the Rotokawa geothermal system, New Zealand," in *New Zealand geothermal workshop 2021*. Auckland, New Zealand: University of Auckland, 8.

Sinclair, B. (1989). in *Lake Rotokawa sulphur deposits*. Editor D. Kear, 13, 89–91. Miner. Depos. New Zeal. Australas. Inst. Min. Metall. Monogr.

Sriaporn, C., Campbell, K. A., Millan, M., Ruff, S. W., Van Kranendonk, M. J., and Handley, K. M. (2020). Stromatolitic digitate sinters form under wide-ranging physicochemical conditions with diverse hot spring microbial communities. *Geobiology* 18, 619–640. doi:10.1111/gbi.12395

Tassi, F., Nisi, B., Cardellini, C., Capecchiacci, F., Donnini, M., Vaselli, O., et al. (2013). Diffuse soil emission of hydrothermal gases (CO2, CH4, and C6H6) at Solfatara crater (Campi Flegrei, southern Italy). *Appl. Geochem.* 35, 142–153. doi:10.1016/j.apgeochem.2013.03.020

Taussi, M., Nisi, B., Pizarro, M., Morata, D., Veloso, E. A., Volpi, G., et al. (2019). Sealing capacity of clay-cap units above the Cerro Pabellón hidden geothermal system (northern Chile) derived by soil CO2 flux and temperature measurements. *J. Volcanol. Geotherm. Res.* 384, 1–14. doi:10.1016/j.jvolgeores.2019.07.009

Taussi, M., Nisi, B., Vaselli, O., Maza, S., Morata, D., and Renzulli, A. (2021). Soil Co2 flux and temperature from a new geothermal area in the cordón de inacaliri volcanic complex (northern Chile). *Geothermics* 89, 101961. doi:10.1016/j.geothermics.2020.101961

Troiano, A., Isaia, R., Tramparulo, F. D. A., and Di Giuseppe, M. G. (2021). The Pisciarelli main fumarole mechanisms reconstructed by electrical resistivity and induced polarization imaging. *Sci. Rep.* 11, 1–17. doi:10.1038/s41598-021-97413-1

Umwelt-Geräte-Technik (2012). *PL-300 User's manual*. Available at: https://manualslib.de/manual/493187/Ugt-Pl-300.html (Accessed January 5, 2023).

Wallis, I. C., Bardsley, C., Powell, T., Rowland, J. V., and O'Brien, J. M. (2013). "A structural model for the Rotokawa geothermal field, New Zealand," in *35th New Zealand geothermal workshop: 2013 proceedings* (New Zealand: Auckland Univ Auckland), 17–20.

Whelley, P. L., Jay, J., Calder, E. S., Pritchard, M. E., Cassidy, N. J., Alcaraz, S., et al. (2012). Post-depositional fracturing and subsidence of pumice flow deposits: Lascar Volcano, Chile. *Bull. Volcanol.* 74, 511–531. doi:10.1007/s00445-011-0545-1

Wilson, C. J. N. (1993). Stratigraphy, chronology, styles and dynamics of late Quaternary eruptions from Taupo volcano, New Zealand. *Philos. Trans. R. Soc. Lond. Ser. A Phys. Eng. Sci.* 343, 205 LP–306. Available at: http://rsta.royalsocietypublishing.org/content/343/1668/205.abstract.

Winick, J., Powell, T., and Mroczek, E. (2009). "The natural-state geochemistry of the Rotokawa reservoir," in *New Zealand geothermal workshop proceedings* (New Zealand: Rotorua), 1–8.

Wyering, L. D., Villeneuve, M. C., Wallis, I. C., Siratovich, P. A., Kennedy, B. M., Gravley, D. M., et al. (2014). Mechanical and physical properties of hydrothermally altered rocks, Taupo Volcanic Zone, New Zealand. *J. Volcanol. Geotherm. Res.* 288, 76–93. doi:10.1016/j.jvolgeores.2014.10.008

Zimbone, S. M., Vickers, A., Morgan, R. P. C., and Vella, P. (1996). Field investigations of different techniques for measuring surface soil shear strength. *Soil Technol.* 9, 101–111. doi:10.1016/0933-3630(96)00002-5